

## The Enigmatic Young Low-Mass Variable TWA 30<sup>1</sup>

Dagny L. Looper<sup>2,3</sup>, Subhanjoy Mohanty<sup>4</sup>, John J. Bochanski<sup>5</sup>, Adam J. Burgasser<sup>3,5,6</sup>, Eric E. Mamajek<sup>7</sup>, Gregory J. Herczeg<sup>8</sup>, Andrew A. West<sup>9</sup>, Jacqueline K. Faherty<sup>3,10,11</sup>, John Rayner<sup>2,3</sup>, Mark A. Pitts<sup>2,3</sup>, J. Davy Kirkpatrick<sup>12</sup>

### ABSTRACT

TWA 30 is a remarkable young ( $7 \pm 3$  Myr), low-mass ( $0.12 \pm 0.04 M_{\odot}$ ), late-type star ( $M5 \pm 1$ ) residing  $42 \pm 2$  pc away from the sun in the TW Hydrae Association. It shows strong outflow spectral signatures such as [S II], [O I], [O II], [O III], and Mg I], while exhibiting weak H $\alpha$  emission ( $-6.8 \pm 1.2 \text{ \AA}$ ). Emission lines of [S II] and [O I] are common to T Tauri stars still residing in their natal molecular clouds, while [O III] and Mg I] emission lines are incredibly rare in this same population; in the case of TWA 30, these latter lines may arise from new outflow material colliding into older outflow

---

<sup>1</sup>This paper includes data gathered with the 6.5-m Magellan Telescopes located at Las Campanas Observatory, Chile.

<sup>2</sup>Institute for Astronomy, University of Hawai'i, 2680 Woodlawn Dr, Honolulu, HI 96822, USA; dagny@ifa.hawaii.edu

<sup>3</sup>Visiting Astronomer at the Infrared Telescope Facility, which is operated by the University of Hawaii under Cooperative Agreement no. NCC 5-538 with the National Aeronautics and Space Administration, Office of Space Science, Planetary Astronomy Program

<sup>4</sup>Imperial College London, 1010 Blackett Lab., Prince Consort Road, London SW7 2AZ, UK

<sup>5</sup>MIT Kavli Institute for Astrophysics & Space Research, 77 Massachusetts Ave, Building 37-664B, Cambridge, MA 02139, USA

<sup>6</sup>Center for Astrophysics and Space Science, University of California San Diego, 9500 Gilman Drive, Mail Code 0424, La Jolla, CA 92093, USA

<sup>7</sup>Department of Physics and Astronomy, University of Rochester, P.O. Box 270171; 500 Wilson Boulevard, Rochester, NY 14627-0171, USA

<sup>8</sup>Max-Planck-Institut für extraterrestrische Physik, Giessenbachstrae, 85748 Garching, Germany

<sup>9</sup>Department of Astronomy, Boston University, 725 Commonwealth Ave, Boston, MA 02215, USA

<sup>10</sup>Department of Physics and Astronomy, Stony Brook University, Stony Brook, NY 11794-3800, USA

<sup>11</sup>Department of Astrophysics, American Museum of Natural History, Central Park West at 79th Street, New York, NY 10034, USA

<sup>12</sup>Infrared Processing and Analysis Center, MS 100-22, California Institute of Technology, Pasadena, CA 91125, USA

fronts. The weak H $\alpha$  emission and small radial velocity shifts of line emission relative to the stellar frame of rest (generally  $\lesssim 10 \text{ km s}^{-1}$ ) suggest that the disk is viewed close to edge-on and that the stellar axis may be inclined to the disk, similar to the AA Tau system, based on its temporal changes in emission/absorption line strengths/profiles and variable reddening ( $A_V = 1.5\text{--}9.0$ ). The strong Li absorption ( $0.61 \pm 0.13 \text{ \AA}$ ) and common kinematics with members of the TWA confirm its age and membership to the association. Given the properties of this system such as its proximity, low mass, remarkable outflow signatures, variability, and edge-on configuration, this system is a unique case study at a critical time in disk evolution and planet-building processes.

*Subject headings:* Galaxy: open clusters and associations: individual (TW Hydrae Association) – stars: circumstellar matter, stars: pre-main-sequence – stars: evolution – stars: individual (2MASS J11321831–3019518, TWA 30) – stars: low-mass, brown dwarfs

## 1. Introduction

Over the past 30 years, a universal but complex paradigm of star formation has been developed through many observations and theoretical breakthroughs (e.g., Shu et al. 1987; Hartmann 1998). Briefly, the stellar birth process begins with the gravitational collapse of material within giant molecular cloud complexes (Class 0 objects; Adams et al. 1987) and progresses as the embedded protostar accretes material from an enshrouding infall envelope (Class I), with this transition lasting  $\sim 200 \text{ kyr}$  (Enoch et al. 2008). As the gas clears, the revealed protostar continues to accrete from a circumstellar disk of material (Class II, Classical T Tauri stars, cTTS; Appenzeller & Mundt 1989). By  $\sim 10 \text{ Myr}$ , accretion ceases (Fedele et al. 2009; Wyatt et al. 2003), and the object is now a pre-main sequence star, possibly with a debris disk (Class III and later) capable of assembling terrestrial planets over timescales of 10–100 Myr (Chambers 2004). This process from cloud core to pre-main sequence star is marked by a wide array of dynamic phenomena, including outflows and accretion.

Recent evidence suggests that the accretion processes at work in Class II systems operate in the regime of very low-mass stars and brown dwarfs as well (e.g., White & Basri 2003; Mohanty et al. 2005). Accretion rates scale roughly as  $\dot{M} \sim M^2$  (Muzerolle et al. 2003; Natta et al. 2004; Calvet et al. 2004; Mohanty et al. 2005; Alexander & Armitage 2006), meaning lower mass systems should display weaker signatures of accretion. Forbidden emission lines (FELs) in optical spectra, arising from low-density optically thin gas, have been used to identify a handful of outflows originating from very low-mass stars and brown dwarfs (e.g., Fernández & Comerón 2001; Muzerolle et al. 2003; Luhman 2004; Mohanty et al. 2005). Only five young brown dwarfs have had their outflows spatially resolved – three optical jets (via spectroastrometry; Whelan et al. 2005, 2007, 2009) and two molecular outflows (via direct imaging; Phan-Bao et al. 2008; Bourke et al.

2005). Identification of such systems is hampered not only by their intrinsic faintness but also by the distances ( $d > 120$  pc) to the nearest star-forming regions (e.g., Sco-Cen, Taurus, Orion), making it difficult to resolve structure on the scales of disks ( $\sim 10$ – $100$  AU) and jets (a few hundred AU). Hence, progress in understanding the size, morphology, and energetics of jets powered by very low-mass stars and brown dwarfs is limited.

Fortunately, the recent identification of new low-mass members of the nearby TW Hydrae Association (TWA) may provide more ideal systems for studies of disk and jet structures in this mass regime. Indeed, one of the three brown dwarfs with a resolved optical jet, 2MASSW J1207334–393254 (2M1207AB, also known as TWA 27AB; Gizis 2002; Chauvin et al. 2004), is a member of the TWA. The namesake of the TWA, TW Hydrae, was the first cTTS found in isolation (Henize 1976) – located only  $54 \pm 6$  pc from the Sun (van Leeuwen 2007), 23 degrees above the Galactic Plane and far from any molecular cloud (Herbig 1978; Rucinski & Krautter 1983; Tachihara et al. 2009). More than a decade after the discovery of TW Hydrae, de la Reza et al. (1989) and Gregorio-Hetem et al. (1992) found four more T Tauri stars in the same vicinity by using the IRAS Point Source Catalog and targeting stars with infrared excess. Based on their common X-ray activity, Kastner et al. (1997) postulated that these five objects formed a physical association of young stars, which they termed the TW Hydrae Association. Soon after, targeted surveys using ROSAT All-Sky Survey (RASS) data (Sterzik et al. 1999; Webb et al. 1999; Zuckerman et al. 2001), kinematic surveys (Song et al. 2003; Scholz et al. 2005), and photometric near-infrared (NIR) surveys (Gizis 2002;Looper et al. 2007) discovered several more members, bringing the total to 23 confirmed systems (Mamajek 2005), of which five contain brown dwarfs.

These systems share similar kinematics and indicators of youth such as strong chromospheric activity and, for late-K to M type members, Li I  $\lambda 6708$  absorption. Isochronal ages derived from the Hertzsprung-Russell diagram yield age estimates of  $\sim 8$  Myr for the TWA (Soderblom et al. 1998; Webb et al. 1999; Weintraub et al. 2000; Barrado y Navascués 2006). At an average distance of 53 pc (Mamajek, in preparation), the TWA is the nearest association containing actively accreting young stars<sup>1</sup>, making it an attractive target for studying planet formation and the evolution of circumstellar disks. Moreover, members of the TWA span a range of disk evolutionary stages, with some members showing signs of actively accreting disks, passive/non-accreting disks, or debris disks, while other members show no signs of circumstellar material (e.g., Jayawardhana et al. 1999; Low et al. 2005).

We have undertaken a survey to identify additional low-mass members to the TWA, which could provide important new case studies of accretion and outflow in substellar-mass objects residing at close distances ( $\sim 50$  pc). In this paper, we report the discovery of a new, low-mass member of the TWA, 2MASS J11321831–3019518, which we term TWA 30. Its membership is confirmed by its kinematics, Li I  $\lambda 6708$  absorption strength, and signatures of a low-gravity photosphere. TWA 30

---

<sup>1</sup>Although, a recently identified young brown dwarf, 2MASS J0041353–562112, shows signs of accretion and may be a possible  $\beta$  Pic or Tuc-Hor member, placing it at  $\sim 35$ – $50$  pc (Reiners 2009).

has strong forbidden lines of [O I], [O II] and [S II] within  $30 \text{ km s}^{-1}$  of the stellar rest velocity, possibly indicating an outflow from a nearly edge-on system. The presence of [O III] and Mg I in the spectrum of TWA 30 are extremely rare for a cTTS and have not been observed before in a young system residing outside of its natal molecular cloud. The fluctuating continua levels from both the optical and the NIR spectra suggest that they may be affected by highly variable reddening on timescales of a day to several weeks. In § 2, we describe the discovery and observations of TWA 30; in § 3, we analyze the kinematics, spectral morphology, emission/absorption lines, X-ray activity, and estimate an age and mass of TWA 30; in § 4, we discuss evidence for this system having an inclined stellar axis to an edge-on disk and update the disk fraction of the TWA; finally in §5, we give our conclusions.

## 2. Observations

### 2.1. Discovery

We searched for new members of the TWA that appear in the RASS X-ray Faint Source Catalog (Voges et al. 2000) over the right ascension (RA) range  $10^h.5 - 12^h.5$  and declination (DEC) range  $-25^\circ$  to  $-40^\circ$ , with magnitudes of  $7.5 < J < 10$  in the Two Micron All-Sky Survey (2MASS) Point Source Catalog (PSC; Cutri et al. 2003; Skrutskie et al. 2006). Previous searches of RASS data for TWA members (Webb et al. 1999; Zuckerman et al. 2001) have relied on the X-ray Bright Source Catalog (Voges et al. 1999), with the exception of the study by Sterzik et al. (1999), which examined faint sources in RASS data over a much smaller field of view than our survey. We identified TWA 30 in our sample as a faint X-ray source (1RXS J113217.7–302007) with  $(2.47 \pm 0.96) \times 10^{-2} \text{ counts s}^{-1}$ ,  $J = 9.64$ , and  $J - K_s = 0.88$ . TWA 30 is located in the southwest region of the TWA (a finder chart for it is shown in Figure 1). Further details of our search methodology, spurious candidates, and other new members will be reported in a forthcoming paper.

This source was independently identified by Song et al. (2003) as SSS 113218–3019 on the basis of unpublished optical spectral data. They deduced that it is distant ( $>100 \text{ pc}$ ), and hence likely a member of the Lower Centaurus-Crux region. In the following sections we show evidence that it is nearby and a member of the TWA.

### 2.2. Optical Spectroscopic Data

#### 2.2.1. *MagE Spectroscopy*

TWA 30 was observed nine times with the Magellan Echelle (MagE; Marshall et al. 2008) on the 6.5 m Clay Telescope at Las Campanas Observatory. The details of each observation are recorded in Table 1. MagE is a medium resolution, cross-dispersed echellette, covering the optical

regime from 3,000 to 10,500 Å. The 0′′.7 slit was employed for each observation, corresponding to  $R \equiv \lambda / \Delta\lambda \approx 4100$  with no binning. A flux standard was observed during each run, and ThAr arc calibration images were obtained after each science exposure. The spectrum was reduced with the MASE reduction tool pipeline (Bochanski et al. 2009). Briefly, MASE is written in the Interactive Data Language (IDL) and incorporates the entire reduction and calibration process, including bias subtraction, flat fielding, wavelength and flux calibration. Typical wavelength solutions are accurate to  $\sim 5\text{--}7 \text{ km s}^{-1}$ . The reduced spectrum from 2009 Jan 10 UT is shown in Figures 2, 3, and 4. Three of the spectra were taken on the same night (2008 Nov 26 UT) in sequential exposures and are identical to one another; we show the first spectrum of this series and the other six spectra from different epochs in Figure 5.

### 2.2.2. MIKE Spectroscopy

High resolution spectroscopy was obtained with the Magellan Inamori Kyocera Echelle (MIKE; Bernstein et al. 2003) on 2008 Nov 27 UT. TWA 30 was observed with the red camera and the 0′′.7 slit, with coverage from 4,900 to 9,200 Å and  $R \sim 24,000$ . Binning was set at  $2 \times 2$ . ThAr arcs were obtained after the science exposure, and a flux standard was observed during the night for relative flux calibration. The spectrum was reduced using the MIKE IDL pipeline<sup>2</sup>, producing a calibrated 1D spectrum with wavelength solutions accurate to  $\sim 1\text{--}2 \text{ km s}^{-1}$ .

## 2.3. NIR Spectroscopic Data

We observed TWA 30 eleven times with the SpeX spectrograph (Rayner et al. 2003) on the 3.0 m NASA Infrared Telescope Facility (IRTF) in three modes with the 0′′.5 slit: short cross-dispersed (SXD: 0.8–2.4  $\mu\text{m}$ ;  $R \sim 1200$ ), long cross-dispersed (LXD: 1.9–4.2  $\mu\text{m}$ ;  $R \sim 1500$ ), and prism (0.7–2.5;  $R \sim 150$ ). Details of these observations are listed in Table 1. Observations of a nearby A0 V star for telluric correction were made immediately after each observation along with internal flat-field and argon arc lamp frames for calibrations. Reductions were carried out using the Spextool package version 3.4 (Cushing et al. 2004; Vacca et al. 2003). The LXD data were first combined at each nod position; reductions using the Spextool package were otherwise standard.

## 2.4. Imaging

We observed TWA 30 at the Cerro Tololo 4.0 m Blanco telescope on 2008 Dec 13 UT as part of an ongoing brown dwarf astrometric program. The Infrared Side Port Imager (ISPI;

---

<sup>2</sup>The pipeline is available at <http://web.mit.edu/~burles/www/MIKE/>.

van der Blik et al. 2004) was used along with the  $J$ -band filter. The detector has a  $\sim 10$  arcmin field of view with a  $0''.3$  pixel plate scale. Three images of 10 s exposures using 3 co-adds were obtained at each of the three dither positions. Dark frames and domeflats were obtained at the start of each evening. The raw images were median-combined to produce sky frames, which were then subtracted from the raw data. The subsequent reduction procedures were based on the prescriptions put together by the ISPI team<sup>3</sup>, utilizing a combination of IRAF routines as well as publicly available software packages: WCSTOOLS and SWARP. Each image was flat-fielded, corrected for bad pixels, and flipped to orient N up and E to the left using the IRAF routine *osiris* in the *cirred* package. Individual point sources were selected in each image using the IDL routine *find* and then input into the WCSTOOLS task *imwcs*, which matches stars to the 2MASS PSC. Once an initial world coordinate system (WCS) was set, we used the IRAF routine *ccmap* to correct for the distortion prominent across the ISPI detector. The final WCS residuals against 2MASS were  $\sim 0.1$  pixels in both the X and Y axes. We used the software package *swarp* to shift and add the 3 reduced dither positions and then used this final science frame to perform the astrometry. Final RA, DEC coordinate positions of 11h 32m 18.19s,  $-30^\circ 19' 51.8''$  (equinox J2000) were determined using the IRAF routine *wcstran*, which combines the standard WCS parameters with the higher order distortion corrections calculated with *ccmap*.

### 3. Analysis

#### 3.1. Kinematics

TWA 30 has proper motion estimates in the USNO-B1.0 catalog (Monet et al. 2003) and the SSS catalog (Hambly et al. 2001a,b,c) of  $\mu_\alpha$ ,  $\mu_\delta$  of  $-86 \pm 5$ ,  $-24 \pm 11$  and  $-81 \pm 9$ ,  $-28 \pm 9$  mas yr<sup>-1</sup>, respectively. It is also listed in the UCAC3 catalog (Finch et al. 2010) as 3UCAC 120-147008 with a proper motion of  $\mu_\alpha$ ,  $\mu_\delta$  of  $-89.6 \pm 1.3$ ,  $-25.8 \pm 1.3$  mas yr<sup>-1</sup>. We adopt this latter measurement, which has the smallest errors, as the proper motion for TWA 30.

We determined the radial velocity (RV) of TWA 30 by measuring the line centers of H $\alpha$  and photospheric absorption lines in the MIKE spectrum (Li I  $\lambda 6708$ , K I  $\lambda 7699$ , and Na I  $\lambda 8183$ )<sup>4</sup>, yielding a heliocentric RV of  $12.3 \pm 1.5$  km s<sup>-1</sup> (Table 2). The uncertainty was calculated as the  $1\sigma$  standard deviation in the measurements. To examine the RV variation over time, we calculated RVs from the nine lower resolution MagE spectra by cross-correlating each spectrum with the M6 SDSS template from Bochanski et al. (2007) using the *xcorl* package in IDL (Mohanty & Basri 2003; West & Basri 2009). Our analysis included the wavelength region from 6600 Å to 7200 Å that encompasses the TiO molecular bandhead that begins at 7056 Å. We also calculated the

---

<sup>3</sup>See [http://www.ctio.noao.edu/instruments/ir\\_instruments/ispi/](http://www.ctio.noao.edu/instruments/ir_instruments/ispi/).

<sup>4</sup>We follow the convention of referring to lines in the optical regime at their rest velocity in air and round to the nearest integer.

relative radial velocities by cross-correlating each MagE spectrum with the first spectrum taken chronologically on 2008 Nov 26 UT. These RV values indicate a relative uncertainty of  $\sim 2\text{--}3 \text{ km s}^{-1}$ . They are consistent with each other except for the spectrum taken on 2009 March 4 UT (and possibly 2009 May 31 UT), which shows a statistically smaller radial velocity than observed at other epochs (see Table 3).

Since no parallax measurement of TWA 30 is available, we used the convergent point analysis of Mamajek (2005) to estimate its distance. For these calculations, we adopt the mean velocity of the TWA from Mamajek, in preparation based on revised *Hipparcos* astrometry (van Leeuwen 2007) for TWA 1, 4, and 11, as well as the recent ground-based astrometric analyses of 2M1207AB (TWA 27AB; Gizis et al. 2007; Biller & Close 2007; Ducourant et al. 2008). The adopted TWA velocity is  $(U, V, W) = (-10.2, -18.3, -4.9) \text{ km s}^{-1}$ , with uncertainties of  $\pm 0.5 \text{ km s}^{-1}$  in each component. The intrinsic 1D velocity dispersion in the TWA is approximately  $0.8 \text{ km s}^{-1}$  (Mamajek 2005).

Most of the proper motion of TWA 30 is moving towards the TWA convergent point with near zero peculiar motion ( $1.2 \text{ km s}^{-1}$ ), a strong indication of membership. The proper motion of TWA 30 towards the convergent point is consistent with a cluster parallax of  $23.8 \pm 1.2 \text{ mas}$  or a distance of  $42 \pm 2 \text{ pc}$ . This is much closer than the  $>100 \text{ pc}$  spectrophotometric distance quoted by Song et al. (2003). Given the highly variable nature of this object (see §3.2 & §3.3), the kinematic distance is more reliable. The mean distance to TWA members is  $53 \text{ pc}$  (Mamajek, in preparation), with individual members having distances between  $\sim 20 - 80 \text{ pc}$ .

We conclude that both the radial velocity and proper motion are statistically consistent with TWA 30 being a TWA member. Using the stated distance estimate, we derive the inferred tangential velocity and the  $(U, V, W)$  space motion for TWA 30 with respect to the Sun (see Table 2). For the latter we used the procedure of Johnson & Soderblom (1987) with updated galactic coordinate transformations from Murray (1989) and followed the convention that  $U$  is positive towards the Galactic Center ( $l=0, b=0$ ).

## 3.2. Optical Spectroscopy

### 3.2.1. Spectral Morphology

We spectroscopically classified and determined the  $A_v$  of each epoch of optical data from comparison to M3–M5.75  $\eta$  Cha templates (Luhman & Steeghs 2004). This association has a similar age ( $\sim 7 \text{ Myr}$ ; Mamajek et al. 1999; Lawson et al. 2001) to the TWA and should therefore provide a better continuum fit with comparable surface gravities than would comparison to field templates, which have higher surface gravities. These templates are:  $\eta$  Cha 6 (M3),  $\eta$  Cha 12 (M3.25),  $\eta$  Cha 5 (M4),  $\eta$  Cha 9 (M4.5),  $\eta$  Cha 14 (M4.75),  $\eta$  Cha 17 (M5.25),  $\eta$  Cha 18 (M5.5), and  $\eta$  Cha 16 (M5.75). Both template and data were normalized at  $7500 \text{ \AA}$ , which was chosen as a normalization

point due to the small amount of absorption at this wavelength (Kirkpatrick et al. 1991). Then the data were dereddened by increments of  $A_v=0.1$  using the reddening law of Cardelli et al. (1989) (updated in the near-UV by O’Donnell 1994) to provide the best match to the template spectrum over the wavelength range 6000–8000 Å. We set the ratio of total-to-selective extinction  $R_V \equiv A_V / E(B-V)$  to 3.1 (the standard for the ISM), although large grain sizes would have higher  $R_V$  values (e.g., Weingartner & Draine 2001). The spectral features over this regime cover many broadband features typically used to classify M dwarfs such as TiO, VO, and CrH (Kirkpatrick et al. 1991). The best fit to the continuum, by eye, was then chosen, which simultaneously determined the spectral type and  $A_v$ .

The optimal fit of each epoch is overlaid in Figure 6. The spectral type fits of the seven epochs varied between M4 and M5.25, which span timescales of hours to weeks between epochs. The three spectra obtained on 2008 Nov 26 UT have a best fit to the M4.75 template, the spectrum obtained on 2008 Nov 27 UT has a best fit to an M4.5 template; the 2009 Jan 6, 10, and 11 UT spectra have a best fit to an M4 template; and the 2009 Mar 5 and 2009 May 31 UT have a best fit to an M5.25 template. We discuss the possible underlying cause for these changes in spectral type, M4–M5.25, in §4.2.

### 3.2.2. Emission and Absorption Lines

The alkali line strengths of Na I and K I, which are sensitive indicators of surface gravity (Luhman 1999; Martín et al. 1999; Kirkpatrick et al. 2006; Cruz et al. 2009), are weaker in all of the optical spectra of TWA 30 than in the template dwarf spectra, indicating that this object has a lower surface gravity and is therefore younger than field dwarfs of similar spectral type. However, K I  $\lambda 7699$  goes into emission in the 2009 Jan epochs, introducing some uncertainty in using it as a low gravity indicator. We measured the equivalent widths (EW) of these lines along with many permitted and forbidden emission features<sup>5</sup> over our seven epochs of MagE data and report these in Tables 4, 5, and 6 and show them in Figures 2, 3, and 4.

We report the average over all nights of the Li I absorption and the H $\alpha$  emission EW, as these are indicators of age and accretion/chromospheric activity, respectively. The prominent Balmer emission lines are a sign of youth in low-mass stars (West et al. 2008, and references therein). Furthermore, Li is fully depleted within  $\sim 100$  Myr for stars later than spectral type mid-K (Zuckerman & Song 2004), placing an upper limit on the age of TWA 30. It should be noted that for substellar objects with  $M < 0.059\text{--}0.062 M_\odot$ , their core temperatures never become hot enough to destroy Li (Nelson et al. 1993). The Li EW of TWA 30 ( $0.61 \pm 0.13$  Å) is comparable to other TWA M dwarf members (0.40 to 0.65 Å) and stronger than  $\beta$  Pic M dwarf members (Li

---

<sup>5</sup>These lines were identified using the Atomic Line List v2.04 maintained at <http://www.pa.uky.edu/~peter/atomic/> and from Kamiński et al. (2009) and references there-in.

EW < 0.4 Å, age ~12 Myr; Zuckerman & Song 2004).

The FELs of [O I] and [S II] identified in Figures 2 and 3 are present in the spectra of many cTTS and are signs of an outflow and accretion (Muzerolle et al. 2003). These lines are typically associated with [N II] emission, which is only weakly present at 6548 and 6583 Å. We have also identified the high ionization species [O III] and [Fe III], which typically arise in planetary nebulae or winds from the most massive stars. They are rarely seen in cTTS but are detected in the two high accretion rate cTTS: DG Tau (K5, Hartigan et al. 1995; Raga et al. 1996) and XZ Tau B (M1, White & Ghez 2001). The emission of the high-excitation [OIII] line requires extremely high temperatures and low densities, indicative of collisional shock fronts – e.g., bow shocks formed by the jet running into the surrounding ambient medium (Schwartz 1983; Hartigan 1989; Böhm 1995; Raga et al. 1996). Given the general lack of ISM gas in TWA (Tachihara et al. 2009), this medium may consist of older outflow material from TWA 30, which is overtaken and shocked by the fast moving jet.

Similarly, Mg I]  $\lambda$ 4571 is clearly present in our spectra but is rarely seen in the spectra of cTTS. Ercolano et al. (2008) have predicted the presence of Mg I] arising from gas in a circumstellar disk but noted that the detection may be difficult due to the strong continuum at these wavelengths. Mg I] has previously been detected in XZ Tau B (White & Ghez 2001) and the EXor pre-main sequence star VY Tauri (M0; Herbig 1990), which resides in the Taurus-Auriga Cloud.

While TWA 30 has many strong spectral signatures indicating a strong outflow and hence an actively accreting circumstellar disk, it lacks any detectable He I emission at 4471, 6678, and 7065 Å and has weak emission at 5876 Å (see Table 5). He I emission lines are seen in the accreting M4.75–M8 Taurus members in the sample of Herczeg & Hillenbrand (2008) and in the accreting late-M TWA members TWA 27AB (2M1207AB) and TWA 28 (Herczeg et al. 2009). He I is only weakly present in the accreting late-K TWA member TWA 1 and the early-M TWA 3A (Herczeg et al. 2009). He I emission in cTTS is thought to arise both in the infalling funnel flow (broad component) and in the accretion shock region on the stellar surface (narrow component). We propose a scenario for the absence/weakness of the He I lines in our spectra in §4.2.

We have also examined the radial velocity profiles of several FELs, Balmer lines, and absorption features of our MagE spectra (see Figure 7). These profiles have been corrected for the star’s rest velocity (12.3 km s<sup>-1</sup>) and normalized to the continuum at –250 km s<sup>-1</sup>. Of note, the K I  $\lambda$ 7699 line goes from absorption into emission for the three 2009 Jan epochs. A very weak P Cygni profile is seen in the profile of H $\alpha$  at the 2009 Mar epoch. While all seven epochs of data show Na I D  $\lambda$ 5890, 5896 in emission, the last two epochs of data, 2009 Mar 5 and 2009 May 31 UT, have sharp P Cygni profiles in this feature as well, indicating that we are seeing outflowing winds along the line of sight.

### 3.3. NIR Spectroscopy

#### 3.3.1. Spectral Morphology and Reddening

TWA 30 was observed over several epochs spanning nearly seven months using 0.9–2.4  $\mu\text{m}$  spectroscopy. As we did not have a comprehensive set of young (low-gravity) early-to-late M templates in the NIR, we have used field templates and carried out the same spectral typing and  $A_v$  determination as before in the optical data analysis. In Figure 8, we show our eight epochs of NIR data normalized in the  $K$ -band, which are not taken concurrently with our optical data. From these spectra we have determined spectral types and  $A_v$  measurements for all eight epochs (see Table 7) by dereddening our spectra to the following field templates<sup>6</sup> – Gl 213 (M4 V), Gl 51 (M5 V), Gl 406 (M6 V), vB 8 (M7 V), vB 10 (M8 V). These spectra show a large variability in the amount of reddening present ( $A_v=1.5$ –9.0), which is also correlated with the dereddened spectral types. The epoch with the least amount of reddening, 2009 Feb 2, has the earliest spectral type: M4.5, while the epoch with the highest amount of reddening, 2009 May 20, has the latest spectral type: M6. We outline a possible cause for the changing spectral types in both the optical (M4–M5.25) and NIR (M4.5–M6) in §4.2. Given the variability in spectral type in both the optical and NIR regimes, we adopt a spectral type of  $M5 \pm 1$ .

We have combined the first of these epochs, 2008 Dec 4 UT, with our only longer wavelength (1.9–4.20  $\mu\text{m}$ ) spectroscopic data from 2008 Dec 5 UT. A significant amount of reddening is observed in some of our spectra on day-timescales; however, the  $K$ -band ( $\sim 1.9$ –2.4  $\mu\text{m}$ ) overlap between these two datasets is virtually identical. We compare this wider spectral energy distribution to the M5 field template, Gl 51, in Figure 9. Both spectra have been normalized in  $K$ -band (at 2.1  $\mu\text{m}$ ), showing that TWA 30 is redder than the M5 template, although the longer wavelength  $L$ -band is less affected and matches the template reasonably well. We have chosen an M5 for comparison, as when we dereddened this spectrum the M5 template provided the best fit in spectral slope.

We have also measured spectrophotometry on these data to determine 2MASS  $JHK_s$  colors, as well as on our two lower resolution NIR spectra from 2009 Jun 28 and 29 UT, and report these in Table 7 along with the 2MASS PSC measurements from 1999 Mar 24 UT. The epoch of our data with the least amount of reddening, 2009 Feb 2 ( $A_v=1.5$ ), has  $JHK_s$  magnitudes very similar to those from the 2MASS PSC ( $\Delta = 0.01$ –0.15 mag) epoch. While these spectra have been flux calibrated with nearby A0 V stars, they have not been absolutely flux calibrated with photometry, and therefore do not take into account slit losses. Rayner et al. (2009) estimate that in photometric conditions absolute spectrophotometry performed on SpeX spectra calibrated with nearby A0 V stars are accurate to 10%, while relative spectrophotometry are accurate to a few percent.

---

<sup>6</sup>All template spectra were obtained from [http://irtfweb.ifa.hawaii.edu/~spex/IRTF\\_Spectral\\_Library/index.html](http://irtfweb.ifa.hawaii.edu/~spex/IRTF_Spectral_Library/index.html). These spectra were taken with the same set-up but using the 0'3 slit, instead of the 0'5 slit we employed for our observations.

The colors calculated from these measurements appear to be accurate between our SXD and prism spectra (Table 7), with identical  $H - K_s$  colors and similar  $J - H$  ( $\Delta = 0.06$  mag) colors. These values are shown in  $JHK_s$  color space in Figure 10. Only the 2MASS PSC colors of TWA 30 lie along the dwarf track. All other epochs lie along the reddening vector described by Cardelli et al. (1989). The sparse coverage of our data shows a full cycle over a six month period, however, the rapid increase in  $A_v$  over the period 2009 May 14–20 may indicate that the cycles are much shorter if this behavior is periodic.

### 3.3.2. Emission and Absorption Lines

As seen in the optical data, typical surface gravity indicators such as the alkali metal lines, K I and Na I, are weaker in TWA 30 than in the field M5 template (see Figures 9 and 11). While H Balmer emission in the optical spectrum of TWA 30 is prevalent, H Paschen (Pa) is in *absorption* in the NIR, with the exception of Pa  $\gamma$ , which is seen in emission in our lower resolution SXD data (see Figure 9). A typical indicator of on-going accretion, H Brackett  $\gamma$  can be seen only weakly in emission at  $2.166 \mu\text{m}$  in the  $K$ -band spectrum of the 2008 Dec 4 UT data and is absent in the 2008 Dec 15 and 2009 Feb 2 UT data (see Figure 11).

## 3.4. Estimated Mass and Age

To derive the stellar mass and age we have used two estimates of the spectral type: (1) using the 2MASS colors, which imply a spectral type of  $\sim\text{M4.5}$ , although this probably includes accretion continuum excess emission (see §4.2) and (2) using the latest NIR spectral type, M6, which likely has the least accretion continuum excess (see §4.2), although the spectral type may be slightly too late due to our use of field templates for the NIR data.

For the first estimate, we assume that the 2MASS data point ( $K_s=8.77 \pm 0.02$  mag) has  $A_V, A_K = 0$ . From the  $T_{eff}$  scale<sup>7</sup> for cTTS of Luhman et al. (2003), a spectral type of M4.5 gives an effective temperature of  $3200 \pm 100$  K. The bolometric correction in  $K$ -band ( $BC_K$ ) from Golimowski et al. (2004) begins at spectral type M6, yielding  $BC_K = 3.03 \pm 0.13$  mag for M6 and  $BC_K = 3.06 \pm 0.13$  mag for M7. Although M4.5 is earlier than the beginning of this relation, the change in  $BC_K$  over 1 spectral type ( $\Delta = 0.03$  mag) is small in comparison to the root-mean-square (RMS) in the uncertainty (0.13 mag). We therefore adopt a value of  $BC_K = 3.0 \pm 0.1$  mag on the CIT photometric system. Applying the transformation of Carpenter (2001), 2MASS  $K_s = \text{CIT } K - 0.024$  mag, with negligible uncertainties and a color term of zero. Hence, 2MASS  $K_s = 8.77 \pm 0.02$  mag transforms into CIT  $K = 8.79 \pm 0.02$  mag. For a distance of  $42 \pm 2$  pc (the kinematic distance), the distance modulus is  $3.12 \pm 0.10$  mag, yielding CIT  $M_K = 5.67 \pm 0.10$  mag.

---

<sup>7</sup>Luhman & Muench (2008) estimate an uncertainty of  $\sim 100$  K in this relation.

Applying the bolometric correction yields  $M_{bol} = 8.7 \pm 0.1$  mag. Adopting the IAU standard of  $M_{bol,\odot} = 4.75$  mag,  $\log L_{bol}/L_{bol,\odot} = -1.58 \pm 0.04$  dex. With this  $T_{eff}$  and  $L_{bol}$ , the evolutionary models of Baraffe et al. (1998) give an age of 10 Myr and a mass of  $0.16 M_{\odot}$ .

For the second estimate, we use the latest NIR spectral type derived, M6, in 2009 May 14 and 20 with the corresponding 2MASS  $K_s$  and  $A_V$  estimates listed in Table 7. Using  $A_K/A_V=0.112$  (Rieke & Lebofsky 1985) and the same CIT  $K$  transformation as listed above to correct the NIR magnitudes of these two epochs, we find CIT  $K$  ( $A_K=0$ ) =  $9.05 \pm 0.04$  mag. With the same distance modulus as above, CIT  $M_K = 5.93 \pm 0.11$  mag. The  $BC_K$  correction from Golimowski et al. (2004) for an M6 is  $3.03 \pm 0.13$  mag, yielding  $M_{bol} = 9.0 \pm 0.2$  mag and  $\log L_{bol}/L_{bol,\odot} = -1.70 \pm 0.08$  dex. The  $T_{eff}$  scale of Luhman et al. (2003) for an M6 gives  $T_{eff} = 3000 \pm 100$  K. With this  $T_{eff}$  and  $L_{bol}$ , the evolutionary models of Baraffe et al. (1998) give an age of 4 Myr and a mass of  $0.08 M_{\odot}$ .

As these two spectral types and NIR photometric measurements cover nearly the full range of our measurements, the age of TWA 30 likely lies somewhere between these extremes. The mass inferred from the optical data is likely an overestimation, due to the inclusion of accretion luminosity, while the age inferred from the NIR data is likely an underestimation due to our use of field templates instead of young templates to infer the NIR spectral type. Given these uncertainties, we adopt an age of  $7 \pm 3$  Myr and a mass of  $0.12 \pm 0.04 M_{\odot}$ . This age estimate agrees with the estimated age of the TWA ( $\sim 8$  Myr), and the mass estimate places it near the substellar boundary at  $\sim 0.08 M_{\odot}$  (Chabrier & Baraffe 2000).

### 3.5. X-ray Activity

The RASS Faint Source Catalog lists an X-ray detection of  $(2.5 \pm 1.0) \times 10^{-2}$  counts  $s^{-1}$  at a distance of  $17''.6$  from the 2MASS epoch position of TWA 30. The hardness ratio, HR1, is  $(A-B)/(A+B)$  where band-A covers 0.1–0.4 keV (soft X-rays) and band-B covers 0.5–2.0 keV (hard X-rays). The conversion factor, CF, from counts  $s^{-1}$  to X-ray flux ( $\text{erg cm}^{-2} \text{s}^{-1}$ ) for RASS data of late-type stars is derived by Fleming et al. (1995) as  $CF = (8.31 + 5.30 \times HR1) \times 10^{-12} \text{ erg cm}^{-2} \text{ s}^{-1}$ . The CF for TWA 30 is thus  $7.25 \times 10^{-12} \text{ erg cm}^{-2} \text{ s}^{-1}$  and when combined with the RASS count rate, yields an X-ray flux of  $F_X = 1.8 \times 10^{-13} \text{ erg cm}^{-2} \text{ s}^{-1}$ . With an adopted distance of 42 pc, we then derive  $\log L_X = 28.6$  dex. From the average bolometric luminosity calculated above ( $\log L_{bol}/L_{bol,\odot} = -1.64 \pm 0.09$  dex;  $L_{bol} = 8.8 \times 10^{31} \text{ erg s}^{-1}$ , assuming  $L_{bol,\odot} = 3.85 \times 10^{33} \text{ erg s}^{-1}$ ), this yields  $\log L_X/L_{bol} = -3.34$  dex. For early to mid-M dwarfs,  $\log L_X/L_{bol}$  saturates at  $\sim -3$  dex (Delfosse et al. 1998). For T Tauri stars, both accreting and non-accreting, down into the BD domain,  $\log L_X/L_{bol}$  ranges from  $\sim -3$  to  $-4$  dex (e.g., the Taurus XMM survey; Güdel et al. 2007), which the value of TWA 30 falls into, i.e., is typical.

## 4. Discussion

### 4.1. The Disk Fraction of the TWA

Our observations provide clear evidence for the presence of an actively accreting disk and outflow around TWA 30; however, it is not the only disk-bearing low-mass source in the TWA. Low et al. (2005) measured a 25% disk fraction from a survey of 24 candidate TWA members observed from *Spitzer Space Telescope* mid-IR measurements, including two M1 dwarfs (TWA 7 and TWA 13, the latter of which has been discounted by Plavchan et al. 2009). Other M dwarf members – TWA 14 (M0.5) and TWA 5A (M2.5) – have indications of passive circumstellar disks such as broad asymmetric Balmer emission (Muzerolle et al. 2001; Mohanty et al. 2003) but lack NIR excess emission (however, Jayawardhana et al. 1999 find a modest  $10\ \mu\text{m}$  excess emission for TWA 5A). Two of three substellar systems observed in the mid-IR – TWA 28 and TWA 27A (2M1207A), and possibly TWA 27B (Mohanty et al. 2003; Sterzik et al. 2004; Riaz et al. 2006; Morrow et al. 2008; Riaz & Gizis 2008; Herczeg et al. 2009) – also exhibit signatures of IR excess, accretion and outflow, indicating that the same processes occur in low-mass stars and brown dwarfs (Whelan et al. 2007; Herczeg et al. 2009).

With the addition of TWA 30 as a disk-bearing low-mass member of the TWA, we updated the disk fraction of the TWA considering the following systems listed in Mamajek (2005) as *bona fide* members: TWA 1–11, 13–16, 20, 21, 23, 25–28 (see Torres et al. 2008 and Lawson & Crause 2005 for slightly different membership lists). While we consider TWA 29 (DENIS J124514.1–442907) to be a potential member, no mid-IR observations have yet been reported so we do not include it in our census. Of these systems, many of which are known binaries (e.g., Brandeker et al. 2003), mid-IR observations (listed above) have confirmed circumstellar disks around TWA 1, 3AB, 4AB, 7, 11A, 27A(B), and 28 (shown in RA/decl space in Figure 12). Including TWA 30 increases the disk-bearing population to 8 of 23 systems, or  $35^{+11}_{-8}\%$ . This is a 40% increase (at  $\gtrsim 1\sigma$ ) to the estimate provided by Low et al. (2005).

### 4.2. An Inclined Stellar Axis to an Edge-On Disk?

There are seven striking features of the TWA 30 system that any scenario must explain:

1. The presence of a large number of FELs indicative of jets, with line-center velocities both blue- and red-shifted with respect to the stellar radial velocity but by very small amounts (generally  $\lesssim 10\ \text{km s}^{-1}$ );
2. Temporal variations in the NIR colors and spectrum, with increasing reddening associated with decreasing NIR flux;

3. Temporal variations in the reddening of the optical spectrum as well;
4. Temporal variations in the underlying optical and NIR spectral types inferred after reddening effects are removed, with the earliest spectral type (optical: M4, NIR: M4.5 – non-contemporaneous) associated with the lowest reddening and with the latest type (optical: M5.25, NIR: M6 – non-contemporaneous) associated with the highest reddening;
5. Changes in the equivalent widths of the optical photospheric absorption lines of Li I and K I, with the least absorption when the optical spectral type is earliest;
6. The sporadic appearance of P Cygni profiles in the Na I D resonance doublet, and more weakly, in  $H\alpha$ , with the P Cygni profiles being weakest/absent when the absorption in the Li I and K I lines mentioned above is least; and
7. Variations in the equivalent widths of the FELs, with the smallest widths appearing in the last epochs of optical data when the P Cygni profiles are strongest.

#### 4.2.1. Evidence from FELs for an Edge-On Disk

In regards to the first point, jets from accreting cTTS reach velocities<sup>8</sup> of order 200–300  $\text{km s}^{-1}$ . If the FELs in TWA 30 are assumed to trace such a jet, as in other cTTS, then their very low apparent velocities imply a jet that is nearly aligned with the plane of the sky. This is supported by the very low velocities seen even in the [NII] 6583 Å line, which invariably exhibits only a high velocity component in cTTS (Hirth et al. 1997). By extension, the accretion disk, perpendicular to the jet, must be seen very close to edge-on. This conclusion is further supported by the presence of both blue- and red-shifted FELs; significant deviations from an edge-on viewing angle in cTTS produce only blue-shifted FELs, as the disk obscures the receding red-shifted jet lobe (e.g., Whelan et al. 2009). Further evidence for an edge-on geometry from other signatures is discussed further below.

---

<sup>8</sup>The jet velocity is expected to scale roughly as the escape velocity from the object (Masciadri & Raga 2004), which is very similar for a  $0.5 M_{\odot}$  fiducial cTTS and the  $\sim 0.12 M_{\odot}$  TWA 30.

#### 4.2.2. Evidence for Stellar Reddening due to Disk Dust

The occasional yet significant reddening of the NIR spectrum (point 2), accompanied by a simultaneous dimming of the star in NIR bands, is most easily explained as stellar reddening and occultation by disk dust within the line of sight. In the edge-on case, this dust may be entrained with the gas at the base of the outflow / accretion funnel-flow near the inner edge-of the disk, or signify a disk warp produced in this region by the interaction of a tilted stellar magnetosphere with the disk inner edge, as proposed for the cTTS AA Tau (Bouvier et al. 1999, 2003, 2007).

Similarly, the variable reddening observed in the optical spectrum (point 3) may then also be interpreted as extinction/reddening caused by disk dust in the line of sight. Unfortunately, we do not have simultaneous optical photometry to verify this, as possible in the NIR. Nevertheless, the similar relationship between reddening and spectral type in the optical and NIR supports this conclusion, as described further below.

#### 4.2.3. Evidence for Accretion-related Veiling and Variability

In both the optical and NIR, the underlying spectral type varies by similar amounts after the reddening effects are accounted for (point 4): from M4 to M5.25 in the optical (Table 8 and Figures 2, 3, and 4), and from M4.5 to M6 in the NIR (Table 8). For an accreting object, such changes are most easily ascribed to changes in veiling, i.e., changes in the excess continuum emission due to accretion. In this view, the earliest spectral type corresponds to maximum accretion, and the latest spectral type to minimum accretion.

This interpretation is supported by the behavior of the photospheric lines of Li I  $\lambda$ 6708 and K I  $\lambda$ 7699 (point 5). Both show variable absorption: the smallest absorption equivalent widths (indeed, K I goes into emission) are seen in 2009, when the optical spectral type is earliest, while the largest absorption widths occur in 2009 Mar and May, when the optical types are the latest. For photospheric absorption, this cannot be due simply to changes in the stellar continuum (e.g., due to suppression of the continuum by dust occlusion), since the lines and continuum would be equally affected without changing the equivalent width. Instead, it points to a significant enhancement of accretion during this period which partially fills in (veils) the Li I absorption through excess continuum emission and also produces excess line emission in K I. The observed correlation between decreasing absorption strength (i.e., enhanced accretion) and earlier spectral type then confirms that the changes in the underlying optical spectral type are due to veiling effects. By Occam’s razor, the similar variations in the NIR spectral type may then also be attributed to accretion-induced veiling effects. Note that if this veiling interpretation is correct, then the true spectral type of the star is likely to be  $\sim$ M5.25–M6, i.e., the latest and thus least veiling-affected types we see in the optical and NIR. Nevertheless, given the additional complexity introduced by reddening variability (see next sub-section), we have simply adopted  $M5 \pm 1$  which covers the full range seen in the data; a more accurate classification will have to await time-resolved high-resolution spectroscopy.

#### 4.2.4. *Observed Relationship Between Reddening, Accretion and Wind Signatures*

Moreover, we also see the least reddening  $A_V$  in both the optical and the NIR, when the underlying spectral type is earliest, and intermediate (in the optical) to highest (in the NIR)  $A_V$  when the inferred spectral type is the latest (point 4). If the spectral type changes are due to variable accretion and if the extinction is due to dust in the line of sight, as we argue, then this implies that the dust is mostly anti-correlated with accretion. A physical interpretation of this is supplied further below.

P Cygni profiles (point 6) are clear signatures of cool outflowing winds along the line of sight moving towards the observer (e.g., Edwards et al. 2003 and references therein). Their sporadic appearance in the Na I D lines, and once weakly in  $H\alpha$  (2009 Mar, when the Na I D P Cygni profiles are also strongest), implies that the wind from TWA 30 intersects our line of sight only occasionally. Moreover, the P Cygni profiles are strongest in 2009 Mar and May, when the apparent optical spectral type is latest, M5.25, and absorption in photospheric Li I and K I is greatest, i.e., by our above arguments, when the accretion is weakest. Conversely, the P Cygni profiles are weakest/absent in 2009 Jan, when the optical spectral type is earliest, M4, and the Li I and K I absorption is weakest – i.e, when accretion is strongest. It is noteworthy that the Na I D doublet evinces the strongest, somewhat red-shifted emission in the same 2009 Jan spectra. This cannot be explained simply by the absence of *blue*-shifted P Cygni emission, but instead again indicates enhanced accretion when the P Cygni wind signatures are weakest.

There are two possible explanations for this behavior. The first is that the P Cygni profiles are always present at similar strength, but completely filled in by accretion-induced veiling when accretion is strongest. The other is that there is a real weakening of the wind signatures when accretion is strongest. While some veiling of absorption profiles clearly occurs during enhanced accretion (e.g., in Li I), we suggest that the second effect – a real weakening of the wind – is likely to be present as well, due to the following physically-motivated argument.

#### 4.2.5. *A Physical Interpretation: An Inclined Stellar Magnetosphere Interacting with the Disk Inner-Edge*

We have noted earlier that the extinction/reddening signatures, caused by dust in the line of sight, are anti-correlated with accretion, while now we find that the P Cygni wind signatures show the same behavior. Both can be explained simultaneously by the interaction of a tilted stellar magnetosphere interacting with the inner edge of the accretion disk. In this case, accretion is energetically preferred along one half of the inner edge circumference (where the field lines bend inwards towards the star) while outflow is preferred along the other half (where the field lines bend outwards towards the disk). As the star rotates, an observer viewing the disk edge-on along either the top or bottom disk surface would preferentially see outflow and accretion  $180^\circ$  out of phase in time. This is precisely what is seen, for instance, in the cTTS SU Aur (e.g., Johns & Basri 1995),

and would explain the alternating P Cygni wind signatures and enhanced accretion we observe in TWA 30. Furthermore, the interaction of an inclined magnetosphere is expected to create a disk warp on theoretical grounds (Terquem & Papaloizou 2000), which would explain the variable reddening observed in TWA 30. In the case of AA Tau, where such a warp has also been invoked (Bouvier et al. 2003), it appears associated with the accretion funnel flow, i.e., is correlated instead of anti-correlated with the accretion as we observed for TWA 30. However, Terquem & Papaloizou (2000) show that the specific sense of the warp – i.e., whether the warp vertical extension is parallel or anti-parallel to that of the accretion funnel flow or wind – depends on particular assumptions about the nature of the field at the disk inner edge. Hence, a disk warp associated with the wind base is possible as well. In summary, this single physical situation can explain the variable extinction, variable wind signatures, variable accretion, and apparent anti-correlation of the two former with the latter. On the other hand, if only increased veiling were responsible for the disappearance of the wind-related P Cygni profiles during periods of enhanced accretion, we have no obvious reason for the reddening to be anti-correlated with accretion. We therefore propose that there is in fact a real change in the wind signatures. This must be checked through future high-resolution, time-resolved optical spectroscopy, wherein the wavelength-dependent veiling can be characterized in detail.

#### 4.2.6. Further Evidence for an Edge-On Geometry, and Implications for Accreting Gas

We further see that: the P Cygni profiles are strong in Na I D but weak in  $H\alpha$ ; the Na I D absorption is only moderately blue-shifted from the stellar rest-frame (mean  $\sim 25 \text{ km s}^{-1}$ ; Figure 7); and the  $H\alpha$  emission varies by a factor of 1.8 (following the same trend as other accretion signatures – such as veiling and line emission in K I and Na I D – of being enhanced in 2009 Jan compared to 2009 Mar and May). All these are consistent with the edge-on hypothesis. In this geometry, our line of sight intersects the cool dense base of the flow where the resonance lines of Na I and K I are easily excited but not  $H\alpha$ , so we are more sensitive to changes in accretion and outflow in the former lines than in the latter; this is also where a magneto-centrifugal wind has the smallest velocity (and we see an even smaller component of it in our edge-on line of sight; Edwards 2007; Kwan et al. 2007), yielding only a small shift in radial velocity in wind signatures relative to the stellar rest frame.

In this regard, we also note that in many edge-on systems red-shifted, *inverse* P Cygni absorption is seen superimposed on the  $H\alpha$  emission, arising from infalling gas seen against the hotter accretion shock on the stellar surface. No such feature is apparent in our  $H\alpha$  profiles. This may be because the accreting gas is optically thick, completely obscuring the shock region, as supported by the lack of detectable emission in He I at 4471, 6678, or 7065 Å, as well as very weak narrow emission in He I 5876 Å (the strongest line in the series). In cTTS, He I appears to be produced in both the accretion flow, giving rise to a broad component, and in the shock, yielding a narrow component. The absence of a broad He I component in our data is consistent with an edge-on geometry, since this is a high-temperature line that would not be excited at the cool base of the flow.

The absence or extreme weakness of a He I narrow component in the presence of other accretion signatures, further suggests that the shock region is obscured by optically thick accreting gas.

#### 4.2.7. Evidence for Time-Variability in the FELs, and a Physical Interpretation

The scenario sketched so far is consistent with spatial variations alone: the changes in the accretion/outflow/extinction signatures, due to inner-disk interactions with a tilted stellar magnetosphere, occur as the accretion flow, outflow and disk warp rotate into and out of our line of sight. As such, these signatures should be periodic on the scale of the rotation period of the disk inner edge. In cTTS, this is usually on the order of days. Our observations are very poorly sampled at such short periods, and thus remain consistent with this picture of spatial changes alone. We note that the very strong increase in NIR reddening in 2009 May over a period of only 6 days hints at changes on the timescales expected from rotational effects. This will need to be verified by future finely time-sampled monitoring.

However, spatial variability alone cannot be the whole story. Considering the FELs in TWA 30 (point 7), we note first that the equivalent widths of nearly all of these are weakest in the 2009 Mar and May optical data and strongest in the 2009 Jan optical data. This could be explained if the stellar photosphere were severely occulted in 2009 Jan relative to 2009 Mar and May; i.e., if the FELs were seen in 2009 Jan against a much dimmer continuum. However, this appears in contradiction to our argument above, where the optical data indicate that it is 2009 Jan when the  $A_V$  is least (indicating minimum dust reddening and occlusion) and 2009 March and May when the  $A_V$  is intermediate to highest (indicating maximum reddening/occlusion effects). Moreover, the equivalent widths of different FELs change by different amounts, while they should all change by the same proportion if it is the stellar continuum that is being suppressed. The FELs are also expected to arise on scales of at least a few AU from the star, and thus cannot themselves be expected to be affected by any occultation mechanisms operating near the star (e.g., a disk warp).

The only alternative is that the FELs are intrinsically time-variant. FEL time variations may arise as the jet encounters inhomogeneities in its path, or represent temporal changes in the jet launching. If the latter occurs in TWA 30, then the strengthening of the P Cygni profiles in 2009 Mar and May may indicate an actual increase in the outflow rate at these epochs instead of just the outflow rotating into our line of sight. Such a scenario is not inconsistent with the FELs being weakest in these epochs. An FEL can only arise when the critical density of that particular species is reached, at a distance of tens of AUs for cTTS to perhaps a few AU for brown dwarfs (Whelan et al. 2009). At the very least, there must be a time-lag between the observation (via P Cygni profiles) of a strengthening in the wind at its base, and the corresponding increase in the FELs a few AU away, representing the jet travel time. Assuming a fiducial jet velocity of  $\sim 300 \text{ km s}^{-1}$  and a distance of  $\sim 5 \text{ AU}$  to the critical density region, yields a time lag of  $\sim 30$  days.

Our interpretation of the FEL variations is then simply that at some point in the past there was

a strengthening in the outflow, which led (after some time-lag) to the brightening of the FELs in the 2009 Jan spectra. By the time of the 2009 Mar and May spectroscopy, the FELs have faded back to their normal levels. The fact that these epochs coincide with an increase in accretion and wind signatures near the star, respectively, would simply be coincidental. This is a plausible scenario if changes in the latter signatures occur episodically (and maybe periodically) on timescales of days. We note further that, relative to the 2008 Nov data, the FELs in the 2009 Jan data are stronger: in [O I]  $\lambda 6300$  by 49%, in [S II]  $\lambda 6731$  by 165%, and in [N II]  $\lambda 6583$  by 63% (see Table 8). This may be understood by noting that the requisite critical electron density is highest for [O I], smaller for [S II] and least for [N II]. Thus, for a jet whose streamlines diverge (i.e., density decreases) with increasing distance, the [O I] emission region lies closest to the star, [S II] appears further out, and [N II] lies furthest away, as found earlier by Hirth et al. (1997) for cTTS. We thus posit that the past outflow enhancement has nearly reached the [O I] critical region by 2008 Nov but has yet to arrive at the [S II] and [N II] locations; by 2009 Jan the [O I] FELs have plateaued and the outflow enhancement has arrived in the [S II] region, brightening this line considerably, but has not quite reached [N II] yet; and at last, by 2009 Mar and May, the enhancement has passed all these regions, and all the FELs have faded away again.

To clarify this model, multiple observations are needed: finely time-sampled photometry to measure the periodicity of the disk rotation/outflow, mid-IR photometry to detect the disk, mid-IR spectroscopy to detect the presence of silicates and infer grain sizes, high resolution broadband imaging to resolve the disk, high resolution narrowband imaging to resolve the outflows, polarimetry to investigate the dust-disk geometry, spectroastrometry to spatially map the outflow, and sub-mm observations to measure the disk mass. As one of the few very low-mass stars/brown dwarfs for which many of these observations are possible, TWA 30 could prove to be an invaluable case study for accretion and outflow processes at the low-mass end.

## 5. Conclusion

We have identified a new and unusual member of the TW Hydrae Association, TWA 30, which has emission lines of [O I], [O II], [O III], [S II], and Mg I near the stellar rest velocity, indicating it is powering an outflow. The temporal changes in reddening, absorption/emission EWs, and line profiles, particularly for Na I D, suggests a stellar magnetospheric axis inclined with respect to a disk that is viewed nearly edge-on. The presence of forbidden line emission [OIII] and Mg I in the spectra of TWA 30 marks the first time these lines have been seen in a young star not residing in a molecular cloud and are rarely present even amongst cTTS in star formation regions. Both the optical and NIR spectral types appear to vary in accordance with the reddening from M4–M5.25 and from M4.5–M6, respectively, so we have adopted a spectral type of  $M5 \pm 1$ . We suggest that the earlier spectral types are seen at periods of high accretion and include continuum excess emission. The spectral type of TWA 30 therefore might be as late as M5.25–M6. From evolutionary models, we estimate an age of  $7 \pm 3$  Myr and a mass of  $0.12 \pm 0.04 M_{\odot}$ . The close proximity of TWA 30,

$42 \pm 2$  pc, makes it an excellent target for follow-up studies to spatially resolve the outflow and circumstellar disk. With the inclusion of TWA 30, we have updated the disk census of the TWA, finding that  $35_{-8}^{+11}\%$  of observed TWA members still retain their circumstellar disks, a higher ratio than previous estimates.

We thank our anonymous referee whose comments improved the quality of this paper. We are grateful to George Herbig, Mike Cushing, Nathan Smith, Silvia Alencar, Silvie Cabrit, Bo Reipurth, Klaus Hodapp, Brendan Bowler, Kevin Covey, George Wallerstein, and Suzanne Hawley for useful discussions. We also thank our telescope operators at Magellan: Mauricio Martinez, Hernán Nuñez, and Ricardo Covarrubias, and at IRTF: Paul Sears, Bill Golisch, Dave Griep. D.L.L. thanks Dave Sanders and George Herbig for financial support. This research has benefitted from the M, L, and T dwarf compendium housed at DwarfArchives.org and maintained by Chris Gelino, J. Davy Kirkpatrick, and Adam Burgasser. This research has made use of the Atomic Line List v2.04 maintained at <http://www.pa.uky.edu/~simspeter/atomic/>; the SIMBAD database and VizieR catalogue access tool, operated at CDS, Strasbourg, France; and the facilities of the Canadian Astronomy Data Centre operated by the National Research Council of Canada with the support of the Canadian Space Agency. This paper uses data from the IRTF Spectral Library ([http://irtfweb.ifa.hawaii.edu/~simspex/IRTF\\_Spectral\\_Library/index.html](http://irtfweb.ifa.hawaii.edu/~simspex/IRTF_Spectral_Library/index.html)) maintained by John Rayner, Michael Cushing, and William Vacca. This publication makes use of data products from the Two Micron All Sky Survey, which is a joint project of the University of Massachusetts and the Infrared Processing and Analysis Center/California Institute of Technology, funded by the National Aeronautics and Space Administration and the National Science Foundation. This research has made use of the NASA/IPAC Infrared Science Archive, which is operated by the Jet Propulsion Laboratory, California Institute of Technology, under contract with the National Aeronautics and Space Administration. As some spectroscopic follow-up data was obtained from the summit of Mauna Kea, the authors wish to recognize and acknowledge the very significant and cultural role and reverence that this mountaintop has always had with the indigenous Hawaiian community. We are most fortunate to have the opportunity to conduct observations there.

Facilities: IRTF (SpeX), Magellan (MagE), Blanco (ISPI)

Table 1. Spectroscopic Observation Log for TWA 30

Tel./Inst.	$\lambda$ ( $\mu\text{m}$ )	$\lambda/\Delta\lambda$	UT Date <sup>a</sup>	$N \times t$ (s) <sup>b</sup>	Z	Calibrator	Conditions
Magellan/MagE	0.30–1.05	4100	081126–1 <sup>c</sup>	$1 \times 300$	1.4	HR 3454 (WD)	Light Cirrus, 0''5 seeing
Magellan/MagE	0.30–1.05	4100	081126–2 <sup>c</sup>	$1 \times 300$	1.4	HR 3454 (WD)	Light Cirrus, 0''5 seeing
Magellan/MagE	0.30–1.05	4100	081126–3 <sup>c</sup>	$1 \times 300$	1.4	HR 3454 (WD)	Light Cirrus, 0''5 seeing
Magellan/MagE	0.30–1.05	4100	081127	$1 \times 500$	1.5	GD 108 (WD)	Clear, 0''6 seeing
Magellan/MagE	0.30–1.05	4100	090106	$1 \times 500$	1.2	GD 108 (WD)	Clear, 0''8 seeing
Magellan/MagE	0.30–1.05	4100	090110	$1 \times 900$	1.3	GD 108 (WD)	Clear, 0''5 seeing
Magellan/MagE	0.30–1.05	4100	090111	$1 \times 900$	1.3	GD 108 (WD)	Clear, 0''5 seeing
Magellan/MagE	0.30–1.05	4100	090305	$1 \times 750$	1.0	GD 108 (WD)	Clear, 0''5 seeing
Magellan/MagE	0.30–1.05	4100	090531	$1 \times 750$	1.1	EG 274 (WD)	Thin Clouds, 0''9 seeing
Magellan/MIKE	0.49–0.92	27000	081127	$1 \times 500$	1.7	HR 3454 (WD)	Clear, 0''6 seeing
IRTF/SpeX	0.80–2.40	1200	081204	$6 \times 120$	1.7	HD 92678 (A0 V)	Light Cirrus, 0''6 seeing
IRTF/SpeX	1.90–4.20	1500	081205	$20 \times 30$	1.8	HD 92678 (A0 V)	1–2 mags Cirrus, 0''7 seeing
IRTF/SpeX	0.80–2.40	1200	081215	$12 \times 180$	1.7	HD 94741 (A0 V)	Clear, 0''8 seeing
IRTF/SpeX	0.80–2.40	1200	090202	$10 \times 120$	1.6	HD 98949 (A0 V)	Light Cirrus, 0''5 seeing
IRTF/SpeX	0.80–2.40	1200	090514	$6 \times 100$	1.7	HD 89911 (A0 V)	Clear, 0''5 seeing
IRTF/SpeX	0.80–2.40	1200	090515	$8 \times 120$	1.7	HD 110653 (A0 V)	Clear, 0''5 seeing
IRTF/SpeX	0.80–2.40	1200	090520	$8 \times 120$	2.5	HD 98949 (A0 V)	Clear, 0''8 seeing
IRTF/SpeX	0.80–2.40	1200	090616	$6 \times 180$	1.9	HD 98949 (A0 V)	Light Cirrus, 0''7 seeing
IRTF/SpeX	0.70–2.50	150	090628	$6 \times 10$	2.1	HD 98949 (A0 V)	Clear, 0''5 seeing
IRTF/SpeX	0.70–2.50	150	090629	$6 \times 20$	1.9	HD 98949 (A0 V)	Clear, 0''8 seeing
IRTF/SpeX	0.80–2.40	1200	090629	$4 \times 250$	2.5	HD 98949 (A0 V)	Clear, 0''8 seeing

<sup>a</sup>Epochs are denoted as YYMMDD in all tables.

<sup>b</sup>Number of integrations times the integration time.

<sup>c</sup>Three spectra were taken consecutively on 2008 Nov 26, which we denote as 1,2,3.

Table 2. Properties of TWA 30

Parameter	Value	Ref
$\alpha$ (J2000) <sup>a</sup>	11 32 18.31	1
$\delta$ (J2000) <sup>a</sup>	−30 19 51.8	1
$\mu_\alpha$	$−89.6 \pm 1.3$ mas yr <sup>−1</sup>	2
$\mu_\delta$	$−25.8 \pm 1.3$ mas yr <sup>−1</sup>	2
Distance <sup>b</sup>	$42 \pm 2$ pc	3
$v_{tan}$ <sup>b</sup>	$18.6 \pm 1.3$ km s <sup>−1</sup>	3
$v_{rad}$	$12.3 \pm 1.5$ km s <sup>−1</sup>	3
$(U, V, W)$ <sup>b</sup>	$(−10.8, −19.2, −3.6) \pm (0.8, 1.4, 0.9)$ km s <sup>−1</sup>	3
Optical SpT	M5 ± 1	3
Age <sup>c</sup>	$7 \pm 3$ Myr	3
Mass <sup>c</sup>	$0.12 \pm 0.04 M_\odot$	3
$\log L_{bol}/L_\odot$	$−1.64 \pm 0.09$ dex	3
$B^d$	15.6	4
$R^d$	12.9	4
$I^d$	$11.30 \pm 0.03$	5
$J^d$	$9.64 \pm 0.02$	1
$H^d$	$9.03 \pm 0.02$	1
$K_s^d$	$8.77 \pm 0.02$	1
Li EW <sup>e</sup>	$0.61 \pm 0.13$ Å	3
H $\alpha$ EW <sup>f</sup>	$−6.8 \pm 1.2$ Å	3
X-ray	$(2.5 \pm 1.0) \times 10^{-2}$ counts s <sup>−1</sup>	6
HR1	$−0.2 \pm 0.4$	6
HR2	$1.0 \pm 0.6$	6
$\log L_X/L_{bol}$	$−3.34$ dex	3

<sup>a</sup>Coordinates are from the 2MASS Point Source Catalog at epoch 1999 March 24 UT.

<sup>b</sup>Estimated; see §3.1.

<sup>c</sup>See §3.4.

<sup>d</sup>Given in magnitudes. TWA 30 has time variable photometry. See references for further information.

<sup>e</sup>Derived from the average equivalent widths measured from the seven MagE spectra reported in Table 6. The stated error is the  $1\sigma$  standard deviation in the measurement.

<sup>f</sup>Derived from the average equivalent widths measured from the seven MagE spectra reported in Table 4. The stated error is the  $1\sigma$  standard deviation in the measurement.

Note. — References: (1) 2MASS (Skrutskie et al. 2006), (2) Finch et al. (2010), (3) this paper, (4) USNO-A2.0 (Monet & et al. 1998), (5) DENIS (Epchtein et al. 1997), and (6) ROSAT All Sky Survey Faint Source Catalog (Voges et al. 2000).

Table 3. Radial Velocity Measurements for TWA  
30 from MagE Data

UT Date	Abs. RV [km s <sup>-1</sup> ] <sup>a</sup>	Rel. RV [km s <sup>-1</sup> ] <sup>b</sup>
081126–1	15.1	N/A
081126–2	12.5	–1.1
081126–3	13.4	–2.3
081127	11.3	–4.0
090106	16.7	2.1
090110	13.5	–1.8
090111	14.8	0.0
090305	5.9	–8.2
090531	11.0	–6.0

<sup>a</sup>These measurements were made by cross-correlation with radial velocity standards; see §3.1.

<sup>b</sup>These measurements were made by cross-referencing each spectrum to the 081126–1 UT spectrum and determining the relative offset.

Table 4. Equivalent Widths of Balmer Lines for TWA 30

UT Date	$\lambda_{lab}$ (Å)	$\lambda_{obs}$ (Å)	Ion	Flux <sup>a</sup>	EW $\pm 1\sigma$ (Å)	v <sup>b</sup>
081126–1	4102.892	4103.028	H $\delta$	6.3	$-2.7 \pm 1.2$	10
081126–2	4102.892	4102.864	H $\delta$	6.3	$-4.6 \pm 1.5$	–2
081127	4102.892	4103.095	H $\delta$	6.3	$-3.8 \pm 0.6$	15
090106	...	...	H $\delta$	...	...	...
090110	...	...	H $\delta$	...	...	...
090111	...	...	H $\delta$	...	...	...
090305	4102.892	4103.013	H $\delta$	4.9	$-3.1 \pm 0.4$	9
090531	...	...	H $\delta$	...	...	...
081126–1	4341.684	4342.017	H $\gamma$	10.0	$-6.1 \pm 1.0$	23
081126–2	4341.684	4341.914	H $\gamma$	9.0	$-5.1 \pm 1.7$	16
081126–3	4341.684	4342.005	H $\gamma$	9.6	$-5.8 \pm 2.4$	22
081127	4341.684	4341.933	H $\gamma$	9.5	$-5.7 \pm 0.5$	17
090106	...	...	H $\gamma$	...	...	...
090110	4341.684	4341.855	H $\gamma$	9.4	$-5.5 \pm 1.8$	12
090111	...	...	H $\gamma$	...	...	...
090305	4341.684	4341.796	H $\gamma$	6.9	$-4.0 \pm 0.2$	8
090531	...	...	H $\gamma$	...	...	...
081126–1	4862.683	4862.951	H $\beta$	10.3	$-6.7 \pm 0.3$	17
081126–2	4862.683	4862.915	H $\beta$	10.2	$-6.7 \pm 0.2$	14
081126–3	4862.683	4862.909	H $\beta$	12.6	$-8.9 \pm 1.3$	14
081127	4862.683	4862.838	H $\beta$	11.2	$-7.7 \pm 0.2$	10
090106	4862.683	4863.037	H $\beta$	11.5	$-7.5 \pm 2.6$	22
090110	4862.683	4862.863	H $\beta$	10.2	$-6.6 \pm 0.7$	11
090111	4862.683	4862.871	H $\beta$	9.6	$-6.0 \pm 1.2$	12
090305	4862.683	4862.823	H $\beta$	9.4	$-5.9 \pm 0.1$	9
090531	4862.683	4862.816	H $\beta$	8.4	$-4.9 \pm 0.2$	8
081126–1	6564.610	6564.940	H $\alpha$	13.3	$-8.0 \pm 0.1$	15
081126–2	6564.610	6564.857	H $\alpha$	12.9	$-7.6 \pm 0.1$	11
081126–3	6564.610	6564.799	H $\alpha$	11.1	$-5.9 \pm 0.1$	9
081127	6564.610	6564.747	H $\alpha$	12.9	$-8.1 \pm 0.1$	6
090106	6564.610	6564.811	H $\alpha$	12.1	$-6.8 \pm 0.1$	9
090110	6564.610	6564.777	H $\alpha$	12.1	$-6.8 \pm 0.1$	8
090111	6564.610	6564.854	H $\alpha$	13.3	$-8.0 \pm 0.1$	11
090305	6564.610	6564.689	H $\alpha$	9.5	$-4.6 \pm 0.1$	4
090531	6564.610	6564.647	H $\alpha$	10.4	$-5.6 \pm 0.1$	2

<sup>a</sup>The integrated line fluxes are given in units of  $10^{-16}$  erg cm $^{-2}$  s $^{-1}$  and should only be used to calculate relative line fluxes between features in the same spectrum as our data are not photometrically calibrated and hence do not account for slit losses or non-photometric conditions.

<sup>b</sup>These velocities (km s $^{-1}$ ) are not corrected to the stellar rest frame ( $12.3 \pm 1.5$  km s $^{-1}$ ).

Table 5. Equivalent Widths of Selected Non-Balmer Emission Lines for TWA 30

UT	$\lambda_{lab}$ (Å)	$\lambda_{obs}$ (Å)	Ion	Flux <sup>a</sup>	EW $\pm 1\sigma$ (Å) <sup>b</sup>	v <sup>c</sup>
081126–1	3727.090	3727.06	[O II] <sup>d</sup>	11.5	–8.5	–2
081126–2	3727.090	3727.05	[O II] <sup>d</sup>	7.8	–37.5	–3
081126–3	3727.090	3727.02	[O II] <sup>d</sup>	7.1	–24.9	–6
081127	3727.090	3726.94	[O II] <sup>d</sup>	10.8	–15.6	–12
090106	3727.090	3727.29	[O II] <sup>d</sup>	4.2	–17.1	16
090110	3727.090	3727.08	[O II] <sup>d</sup>	7.4	–15.7	–1
090111	3727.090	3727.05	[O II] <sup>d</sup>	4.1	–58.9	–3
090305	3727.090	3727.09	[O II] <sup>d</sup>	10.2	–14.1	0
090531	3727.090	3727.10	[O II] <sup>d</sup>	3.7	–30.2	1
081126–1	3729.880	3729.91	[O II] <sup>d</sup>	6.2	–5.1	2
081126–2	3729.880	3730.08	[O II] <sup>d</sup>	4.9	–14.5	16
081126–3	3729.880	3729.88	[O II] <sup>d</sup>	2.8	–11.7	0
081127	3729.880	3729.92	[O II] <sup>d</sup>	6.7	–9.8	3
090106	3729.880	3729.83	[O II] <sup>d</sup>	2.4	–7.5	–4
090110	3729.880	3729.91	[O II] <sup>d</sup>	4.6	–6.8	2
090111	3729.880	3729.65	[O II] <sup>d</sup>	2.4	–14.8	–19
090305	3729.880	3729.92	[O II] <sup>d</sup>	6.0	–9.7	3
090531	3729.880	3729.88	[O II] <sup>d</sup>	3.5	–26.5	0
081126–1	3934.777	3935.235	Ca II k <sup>e</sup>	10.2	–68.2	35
– – –	3934.777	3933.775	Ca II k <sup>e</sup>	...	...	–76
081126–2	3934.777	3935.271	Ca II k <sup>e</sup>	34.0	–29.7 $\pm$ 6.9	38
– – –	3934.777	3933.509	Ca II k <sup>e</sup>	...	...	–97
081126–3	3934.777	3935.201	Ca II k <sup>e</sup>	5.5	–17.0	32
– – –	3934.777	...	Ca II k <sup>e</sup>	...	...	...
081127	3934.777	3935.172	Ca II k <sup>e</sup>	32.7	–28.4 $\pm$ 1.5	30
– – –	3934.777	3933.389	Ca II k <sup>e</sup>	...	...	–106
090106	3934.777	3935.14	Ca II k <sup>e</sup>	4.0	–50.7	34
– – –	3934.777	3934.143	Ca II k <sup>e</sup>	...	...	–48
090110	3934.777	3935.103	Ca II k <sup>e</sup>	7.2	–30.9	25
– – –	3934.777	3933.953	Ca II k <sup>e</sup>	...	...	–63
090111	3934.777	3935.02	Ca II k <sup>e</sup>	...	–17.8	19
– – –	3934.777	3933.799	Ca II k <sup>e</sup>	...	...	–75
090305	3934.777	3935.204	Ca II k <sup>e</sup>	34.8	–30.2 $\pm$ 1.5	33
– – –	3934.777	3933.886	Ca II k <sup>e</sup>	...	...	–9
090531	3934.777	3935.09	Ca II k <sup>e</sup>	4.4	–17.0	24
081126–1	3969.591	3969.916	Ca II h + He <sup>d</sup>	17.3	–12.2 $\pm$ 2.3	25
081126–2	3969.591	3969.71	Ca II h + He <sup>d</sup>	...	–6.1	26
081126–3	3969.591	3970.100	Ca II h + He <sup>d</sup>	21.7	–15.5 $\pm$ 7.0	38
081127	3969.591	3970.044	Ca II h + He <sup>d</sup>	28.4	–23.3 $\pm$ 2.8	34
090106	3969.591	3969.946	Ca II h + He <sup>d</sup>	26.6	–21.8 $\pm$ 2.7	27
090110	3969.591	3969.907	Ca II h + He <sup>d</sup>	...	–32.0	24
090111	3969.591	3969.99	Ca II h + He <sup>d</sup>	...	–84.6	30
090305	3969.591	3969.973	Ca II h + He <sup>d</sup>	29.0	–24.0 $\pm$ 2.0	29
090531	3969.591	3969.85	Ca II h + He <sup>d</sup>	...	–33.0	29
081126–1	4069.749	4069.918	[S II]	19.3	–15.4 $\pm$ 2.0	13
081126–2	4069.749	4069.829	[S II]	8.40	–5.0 $\pm$ 0.5	6

Table 5—Continued

UT	$\lambda_{lab}$ (Å)	$\lambda_{obs}$ (Å)	Ion	Flux <sup>a</sup>	EW $\pm 1\sigma$ (Å) <sup>b</sup>	$v^c$
081126–3	4069.749	...	[S II]	...	...	...
081127	4069.749	4069.858	[S II]	13.5	$-10.1 \pm 0.6$	8
090106	4069.740	4069.68	[S II]	2.3	-15.4	-4
090110	4069.749	4069.666	[S II]	11.8	$-7.9 \pm 1.6$	-6
090111	4069.749	...	[S II]	...	...	...
090305	4069.749	4069.802	[S II]	9.5	$-6.6 \pm 0.3$	4
090531	4069.749	4069.837	[S II]	8.9	$-6.3 \pm 2.6$	7
081126–1	4077.500	...	[S II]	...	...	...
081126–2	4077.500	...	[S II]	...	...	...
081126–3	4077.500	...	[S II]	...	...	...
081127	4077.500	4077.448	[S II]	5.2	$-2.5 \pm 0.4$	-4
090106	4077.500	4077.57	[S II]	<0.6	< -2.7	5
090110	4077.500	...	[S II]	...	...	...
090111	4077.500	...	[S II]	...	...	...
090305	4077.500	4077.558	[S II]	5.3	$-2.6 \pm 0.3$	4
090531	4077.500	...	[S II]	...	...	...
081126–1	4364.440	4364.966	[O III]	5.4	$-1.2 \pm 0.6$	36
081126–2	4364.440	...	[O III]	...	...	...
081126–3	4364.440	...	[O III]	...	...	...
081127	4364.440	4364.786	[O III]	6.2	$-2.1 \pm 0.4$	24
090106	4364.440	...	[O III]	...	...	...
090110	4364.440	...	[O III]	...	...	...
090111	4364.440	...	[O III]	...	...	...
090305	4364.440	4364.770	[O III]	5.3	$-1.1 \pm 0.2$	23
090531	4364.440	...	[O III]	...	...	...
081126–1	4572.377	4572.388	Mg I]	7.0	$-2.3 \pm 0.4$	1
081126–2	4572.377	4572.490	Mg I]	9.0	$-4.2 \pm 0.4$	7
081126–3	4572.377	4572.481	Mg I]	12.7	$-7.9 \pm 1.0$	7
081127	4572.377	4572.372	Mg I]	8.6	$-3.9 \pm 0.2$	0
090106	4572.377	4572.310	Mg I]	7.4	$-2.9 \pm 0.9$	-4
090110	4572.377	4572.206	Mg I]	7.6	$-3.0 \pm 0.4$	-11
090111	4572.377	4572.235	Mg I]	7.6	$-2.9 \pm 1.0$	-9
090305	4572.377	4572.365	Mg I]	7.5	$-2.8 \pm 0.1$	-1
090531	4572.377	4572.276	Mg I]	6.3	$-1.6 \pm 0.6$	-7
081126–1	4659.350	4659.183	[Fe III]	5.1	$-1.7 \pm 0.2$	-11
081126–2	4659.350	4659.253	[Fe III]	5.1	$-1.3 \pm 0.2$	-6
081126–3	4659.350	...	[Fe III]	...	...	...
081127	4659.350	4659.500	[Fe III]	5.3	$-1.9 \pm 0.1$	10
090106	4659.350	...	[Fe III]	...	...	...
090110	4659.350	4659.590	[Fe III]	5.4	$-1.7 \pm 0.3$	15
090111	4659.350	...	[Fe III]	...	...	...
090305	4659.350	4659.684	[Fe III]	5.0	$-1.2 \pm 0.1$	21
090531	4659.350	...	[Fe III]	...	...	...
081126–1	4756.020	4756.065	[Fe III]	2.3	$-0.2 \pm 0.1$	+3
081126–2	4756.020	...	[Fe III]	...	...	...
081126–3	4756.020	...	[Fe III]	...	...	...

Table 5—Continued

UT	$\lambda_{lab}$ (Å)	$\lambda_{obs}$ (Å)	Ion	Flux <sup>a</sup>	EW $\pm 1\sigma$ (Å) <sup>b</sup>	$v^c$
081127	4756.020	4756.789	[Fe III]	3.0	$-0.5 \pm 0.1$	48
090106	4756.020	...	[Fe III]	...	...	...
090110	4756.020	...	[Fe III]	...	...	...
090111	4756.020	...	[Fe III]	...	...	...
090305	4756.020	4756.644	[Fe III]	2.5	$-0.4 \pm 0.1$	39
090531	4756.020	...	[Fe III]	...	...	...
081126–1	4960.300	4960.380	[O III]	13.2	$-7.8 \pm 0.2$	5
081126–2	4960.300	4960.508	[O III]	15.1	$-9.4 \pm 0.2$	13
081126–3	4960.300	4960.452	[O III]	16.3	$-10.4 \pm 0.7$	9
081127	4960.300	4960.411	[O III]	12.7	$-7.2 \pm 0.1$	7
090106	4960.300	4960.389	[O III]	17.8	$-12.2 \pm 1.8$	5
090110	4960.300	4960.439	[O III]	17.9	$-12.4 \pm 1.0$	8
090111	4960.300	4960.303	[O III]	20.7	$-15.2 \pm 3.7$	0
090305	4960.300	4960.470	[O III]	10.0	$-4.1 \pm 0.1$	10
090531	4960.300	4960.570	[O III]	9.0	$-3.1 \pm 0.4$	16
081126–1	5008.240	5008.261	[O III]	33.6	$-25.1 \pm 0.2$	1
081126–2	5008.240	5008.277	[O III]	31.6	$-23.1 \pm 0.3$	2
081126–3	5008.240	5008.228	[O III]	36.4	$-27.9 \pm 0.6$	–1
081127	5008.240	5008.219	[O III]	33.3	$-24.8 \pm 0.3$	–1
090106	5008.240	5008.78	[O III]	...	$-49.2$	32
090110	5008.240	5008.337	[O III]	34.2	$-25.6 \pm 0.7$	6
090111	5008.240	5008.313	[O III]	32.9	$-24.6 \pm 1.0$	4
090305	5008.240	5008.268	[O III]	18.9	$-10.5 \pm 0.1$	2
090531	5008.240	5008.299	[O III]	18.0	$-9.6 \pm 0.4$	4
081126–1	5877.227	...	He I	...	...	...
081126–2	5877.227	5876.947	He I	3.6	$-0.2 \pm 0.1$	–14
081126–3	5877.227	5877.406	He I	4.0	$-0.6 \pm 0.1$	9
081127	5877.227	5877.451	He I	3.8	$-0.3 \pm 0.1$	11
090106	5877.227	...	He I	...	...	...
090110	5877.227	...	He I	...	...	...
090111	5877.227	...	He I	...	...	...
090305	5877.227	5877.130	He I	4.4	$-0.5 \pm 0.1$	–5
090531	5877.227	5877.381	He I	3.6	$-0.2 \pm 0.1$	8
081126–1	5891.583	5892.387	Na I D <sup>e</sup>	5.1	$-1.6 \pm 0.1$	41
– – –	5891.583	5890.280	Na I D <sup>e</sup>	...	...	–66
081126–2	5891.583	5892.314	Na I D <sup>e</sup>	5.3	$-1.9 \pm 0.1$	37
– – –	5891.583	5890.062	Na I D <sup>e</sup>	...	...	–77
081126–3	5891.583	5892.286	Na I D <sup>e</sup>	5.3	$-1.4 \pm 0.1$	36
– – –	5891.583	5890.193	Na I D <sup>e</sup>	...	...	–71
081127	5891.583	5892.357	Na I D <sup>e</sup>	5.5	$-2.0 \pm 0.1$	39.
– – –	5891.583	5890.000	Na I D <sup>e</sup>	...	...	–81
090106	5891.583	5892.210	Na I D <sup>e</sup>	9.7	$-5.8 \pm 0.7$	32
– – –	5891.583	5890.436	Na I D <sup>e</sup>	...	...	–58
090110	5891.583	5892.171	Na I D <sup>e</sup>	6.4	$-3.3 \pm 0.2$	30
– – –	5891.583	5890.493	Na I D <sup>e</sup>	...	...	–56
090111	5891.583	5892.245	Na I D <sup>e</sup>	6.9	$-3.9 \pm 0.4$	34

Table 5—Continued

UT	$\lambda_{lab}$ (Å)	$\lambda_{obs}$ (Å)	Ion	Flux <sup>a</sup>	EW $\pm 1\sigma$ (Å) <sup>b</sup>	$v^c$
---	5891.583	5890.496	Na I D <sup>e</sup>	...	...	-55
090305	5891.583	...	Na I D <sup>f</sup>	...	...	...
090531	891.583	...	Na I D <sup>f</sup>	...	...	...
081126-1	5897.558	5898.417	Na I D <sup>e</sup>	2.2	-1.3	44
---	5897.558	5895.873	Na I D <sup>e</sup>	...	...	-86
081126-2	5897.558	5898.333	Na I D <sup>e</sup>	2.2	-1.5	39
---	5897.558	5896.308	Na I D <sup>e</sup>	...	...	-64
081126-3	5897.558	5896.938	Na I D <sup>e</sup>	5.0	-1.1 $\pm$ 0.1	36
---	5897.558	5896.938	Na I D <sup>e</sup>	...	...	-32
081127	5897.558	5898.398	Na I D <sup>e</sup>	4.8	-1.3 $\pm$ 0.1	43
---	5897.558	5896.095	Na I D <sup>e</sup>	...	...	-74
090106	5897.558	5898.136	Na I D <sup>e</sup>	7.4	-4.1 $\pm$ 0.7	29
---	5897.558	5896.217	Na I D <sup>e</sup>	...	...	-98
090110	5897.558	5898.106	Na I D <sup>e</sup>	5.9	-2.8 $\pm$ 0.2	28
---	5897.558	5896.452	Na I D <sup>e</sup>	...	...	-56
090111	5897.558	5898.182	Na I D <sup>e</sup>	6.1	-3.0 $\pm$ 0.4	32
---	5897.558	5896.669	Na I D <sup>e</sup>	...	...	-45
090305	5897.558	...	Na I D <sup>f</sup>	...	...	...
090531	5897.558	...	Na I D <sup>f</sup>	...	...	...
081126-1	6302.050	6302.223	[O I]	14.1	-9.2 $\pm$ 0.1	8
081126-2	6302.050	6302.182	[O I]	13.5	-8.9 $\pm$ 0.1	6
081126-3	6302.050	6302.206	[O I]	13.9	-9.2 $\pm$ 0.1	7
081127	6302.050	6302.102	[O I]	14.5	-9.9 $\pm$ 0.1	2
090106	6302.050	6302.068	[O I]	19.4	-14.8 $\pm$ 0.3	1
090110	6302.050	6302.033	[O I]	18.3	-13.7 $\pm$ 0.1	-1
090111	6302.050	6302.114	[O I]	18.0	-13.4 $\pm$ 0.1	3
090305	6302.050	6302.182	[O I]	7.8	-3.2 $\pm$ 0.1	6
090531	6302.050	6302.313	[O I]	7.8	-3.1 $\pm$ 0.1	13
081126-1	6365.540	6365.655	[O I]	6.3	-2.1 $\pm$ 0.1	5
081126-2	6365.540	6365.721	[O I]	6.6	-1.9 $\pm$ 0.1	9
081126-3	6365.540	6365.752	[O I]	6.8	-2.2 $\pm$ 0.1	10
081127	6365.540	6365.530	[O I]	6.9	-2.3 $\pm$ 0.1	-0
090106	6365.540	6365.558	[O I]	7.6	-3.4 $\pm$ 0.1	1
090110	6365.540	6365.507	[O I]	8.1	-3.4 $\pm$ 0.1	-2
090111	6365.540	6365.562	[O I]	7.4	-3.2 $\pm$ 0.1	1
090305	6365.540	6365.717	[O I]	5.5	-0.8 $\pm$ 0.1	8
090531	6365.540	6365.914	[O I]	5.5	-0.9 $\pm$ 0.1	18
081126-1	6549.850	6550.278	[N II]	3.0	-0.2 $\pm$ 0.1	20
081126-2	6549.850	6549.824	[N II]	3.1	-0.2 $\pm$ 0.1	-1
081126-3	6549.850	...	[N II]	...	...	...
081127	6549.850	6550.045	[N II]	3.0	-0.1 $\pm$ 0.1	9
090106	6549.850	6550.119	[N II]	3.2	-0.4 $\pm$ 0.1	12
090110	6549.850	6549.875	[N II]	3.8	-0.4 $\pm$ 0.1	1
090111	6549.850	6549.924	[N II]	3.7	-0.3 $\pm$ 0.1	3
090305	6549.850	6549.632	[N II]	3.2	-0.3 $\pm$ 0.1	-10
090531	6549.850	6549.865	[N II]	3.1	-0.2 $\pm$ 0.1	1

Table 5—Continued

UT	$\lambda_{lab}$ (Å)	$\lambda_{obs}$ (Å)	Ion	Flux <sup>a</sup>	EW $\pm 1\sigma$ (Å) <sup>b</sup>	v <sup>c</sup>
081126–1	6585.280	6585.279	[N II]	5.0	$-0.6 \pm 0.1$	0
081126–2	6585.280	6585.366	[N II]	5.4	$-0.6 \pm 0.1$	4
081126–3	6585.280	6585.170	[N II]	4.8	$-0.5 \pm 0.1$	–5
081127	6585.280	6585.169	[N II]	4.9	$-0.5 \pm 0.1$	–5
090106	6585.280	6585.407	[N II]	5.9	$-1.0 \pm 0.1$	6
090110	6585.280	6585.169	[N II]	5.1	$-0.8 \pm 0.1$	–5
090111	6585.280	6585.377	[N II]	5.8	$-1.0 \pm 0.1$	4
090305	6585.280	6584.912	[N II]	5.1	$-0.3 \pm 0.1$	–17
090531	6585.280	6585.067	[N II]	4.7	$-0.4 \pm 0.1$	–10
081126–1	6718.290	6718.621	[S II]	3.9	$-0.9 \pm 0.1$	15
081126–2	6718.290	6718.504	[S II]	3.5	$-1.0 \pm 0.1$	10
081126–3	6718.290	6718.520	[S II]	3.7	$-1.2 \pm 0.1$	10
081127	6718.290	6718.518	[S II]	3.6	$-1.1 \pm 0.1$	10
090106	6718.290	6718.627	[S II]	5.5	$-2.6 \pm 0.1$	15
090110	6718.290	6718.521	[S II]	5.2	$-2.7 \pm 0.1$	10
090111	6718.290	6718.600	[S II]	5.5	$-2.5 \pm 0.1$	14
090305	6718.290	6718.376	[S II]	2.8	$-0.3 \pm 0.1$	4
090531	6718.290	6718.280	[S II]	3.0	$-0.5 \pm 0.1$	0
081126–1	6732.670	...	[S II]	...	...	...
081126–2	6732.670	6733.000	[S II]	5.0	$-1.5 \pm 0.1$	15
081126–3	6732.670	6733.000	[S II]	5.0	$-1.6 \pm 0.1$	15
081127	6732.670	6732.888	[S II]	5.2	$-1.7 \pm 0.1$	10
090106	6732.670	6732.990	[S II]	7.5	$-4.0 \pm 0.1$	14
090110	6732.670	6732.913	[S II]	7.3	$-3.4 \pm 0.1$	11
090111	6732.670	6732.962	[S II]	6.9	$-3.5 \pm 0.1$	13
090305	6732.670	6733.000	[S II]	3.9	$-0.4 \pm 0.1$	15
090531	6732.670	6732.673	[S II]	4.1	$-0.6 \pm 0.1$	0
081126–1	7157.130	7157.077	[Fe II]	4.7	$-1.0 \pm 0.1$	–2
081126–2	7157.130	7157.067	[Fe II]	4.7	$-1.0 \pm 0.1$	–3
081126–3	7157.130	7157.235	[Fe II]	5.5	$-1.3 \pm 0.1$	4
081127	7157.130	7157.214	[Fe II]	5.5	$-1.3 \pm 0.1$	4
090106	7157.130	7157.215	[Fe II]	6.0	$-1.8 \pm 0.2$	4
090110	7157.130	7157.215	[Fe II]	6.1	$-2.0 \pm 0.1$	4
090111	7157.130	7157.357	[Fe II]	5.9	$-1.7 \pm 0.1$	10
090305	7157.130	7157.116	[Fe II]	4.3	$-0.6 \pm 0.1$	–1
090531	7157.130	7157.088	[Fe II]	4.4	$-0.7 \pm 0.1$	–2
081126–1	7173.980	7174.055	[Fe II]	3.9	$-0.3 \pm 0.1$	3
081126–2	7173.980	7173.893	[Fe II]	4.1	$-0.4 \pm 0.1$	–4
081126–3	7173.980	7173.871	[Fe II]	4.2	$-0.5 \pm 0.1$	–5
081127	7173.980	7174.041	[Fe II]	4.2	$-0.5 \pm 0.1$	3
090106	7173.980	7174.076	[Fe II]	4.4	$-0.7 \pm 0.1$	4
090110	7173.980	7173.923	[Fe II]	4.4	$-0.7 \pm 0.1$	–2
090111	7173.980	7173.910	[Fe II]	4.3	$-0.6 \pm 0.1$	–3
090305	7173.980	7173.874	[Fe II]	4.1	$-0.4 \pm 0.1$	–4
090531	7173.980	7173.596	[Fe II]	3.5	$-0.3 \pm 0.1$	–16

<sup>a</sup>The integrated line fluxes are given in units of  $10^{-16}$  erg cm<sup>–2</sup> s<sup>–1</sup> and should only be used to calculate relative line fluxes between features in the same spectrum as our data are not photometrically calibrated and hence do not account for slit losses or non-photometric conditions.

<sup>b</sup>Some lines were measured by hand and have typical uncertainties of 0.5–3 Å.

<sup>c</sup>These velocities ( $\text{km s}^{-1}$ ) are not corrected to the stellar rest frame ( $12.3 \pm 1.5 \text{ km s}^{-1}$ ).

<sup>d</sup>This line is blended or contaminated.

<sup>e</sup>This line shows both blue- and red-shifted components. The position of the weaker line component is reported but not the flux or EW.

<sup>f</sup>This line has a p Cygni profile.

Table 6. Equivalent Widths of Selected Absorption Lines for TWA 30

UT	$\lambda_{lab}$ (Å)	$\lambda_{obs}$ (Å)	Ion	Flux <sup>a</sup>	EW $\pm 1\sigma$ (Å)	v <sup>b</sup>
081126–1	5330.014	5330.021	Fe I	1.8	0.6 $\pm$ 0.1	0
081126–2	5330.014	...	Fe I	...	...	...
081126–3	5330.014	5329.688	Fe I	2.0	0.3 $\pm$ 0.1	–18
081127	5330.014	5329.742	Fe I	2.2	0.5 $\pm$ 0.1	–15
090106	5330.014	...	Fe I	...	...	...
090110	5330.014	5329.991	Fe I	2.0	0.4 $\pm$ 0.1	–1
090111	5330.014	...	Fe I	...	...	...
090305	5330.014	5329.659	Fe I	1.8	0.6 $\pm$ 0.1	–20
090531	5330.014	5329.668	Fe I	1.7	0.7 $\pm$ 0.1	–19
081126–1	5372.983	...	Fe I	...	...	...
081126–2	5372.983	5373.160	Fe I	1.7	0.3 $\pm$ 0.1	10
081126–3	5372.983	5373.200	Fe I	1.8	0.6 $\pm$ 0.1	12
081127	5372.983	5373.262	Fe I	1.9	0.5 $\pm$ 0.1	16
090106	5372.983	...	Fe I	...	...	...
090110	5372.983	...	Fe I	...	...	...
090111	5372.983	...	Fe I	...	...	...
090305	5372.983	5373.091	Fe I	1.6	0.4 $\pm$ 0.1	6
090531	5372.983	5373.176	Fe I	1.9	0.5 $\pm$ 0.1	11
081126–1	5398.629	5398.770	Fe I	1.6	0.4 $\pm$ 0.1	8
081126–2	5398.629	...	Fe I	...	...	...
081126–3	5398.629	...	Fe I	...	...	...
081127	5398.629	...	Fe I	...	...	...
090106	5398.629	...	Fe I	...	...	...
090110	5398.629	...	Fe I	...	...	...
090111	5398.629	5398.521	Fe I	1.9	0.5 $\pm$ 0.1	–6
090305	5398.629	5398.597	Fe I	1.6	0.4 $\pm$ 0.1	–2
090531	5398.629	...	Fe I	...	...	...
081126–1	5407.278	...	Fe I	...	...	...
081126–2	5407.278	...	Fe I	...	...	...
081126–3	5407.278	...	Fe I	...	...	...
081127	5407.278	5407.324	Fe I	2.1	0.3 $\pm$ 0.1	3
090106	5407.278	...	Fe I	...	...	...
090110	5407.278	5407.136	Fe I	2.5	0.3 $\pm$ 0.1	–8
090111	5407.278	...	Fe I	...	...	...
090305	5407.278	5407.266	Fe I	2.0	0.4 $\pm$ 0.1	–1
090531	5407.278	5407.266	Fe I	2.0	0.4 $\pm$ 0.1	–1
081126–1	5411.276	5411.733	Cr I	2.5	0.3 $\pm$ 0.1	25
081126–2	5411.276	5411.443	Cr I	2.3	0.5 $\pm$ 0.1	9
081126–3	5411.276	...	Cr I	...	...	...
081127	5411.276	5411.307	Cr I	2.4	0.3 $\pm$ 0.1	2
090106	5411.276	...	Cr I	...	...	...
090110	5411.276	5411.713	Cr I	2.3	0.5 $\pm$ 0.1	24
090111	5411.276	...	Cr I	...	...	...
090305	5411.276	...	Cr I	...	...	...
090531	5411.276	...	Cr I	...	...	...
081126–1	6123.912	6124.077	Ca I	2.6	0.5 $\pm$ 0.1	8

Table 6—Continued

UT	$\lambda_{lab}$ (Å)	$\lambda_{obs}$ (Å)	Ion	Flux <sup>a</sup>	EW $\pm 1\sigma$ (Å)	$v^b$
081126–2	6123.912	6123.961	Ca I	2.8	0.4 $\pm$ 0.1	2
081126–3	6123.912	6124.128	Ca I	2.8	0.3 $\pm$ 0.1	11
081127	6123.912	6124.148	Ca I	2.8	0.3 $\pm$ 0.1	12
090106	6123.912	...	Ca I	...	...	...
090110	6123.912	6123.958	Ca I	2.8	0.4 $\pm$ 0.1	2
090111	6123.912	6124.206	Ca I	2.7	0.4 $\pm$ 0.1	14
090305	6123.912	6123.981	Ca I	2.8	0.3 $\pm$ 0.1	3
090531	6123.912	6123.982	Ca I	2.7	0.4 $\pm$ 0.1	3
081126–1	6709.660	6710.010	Li I	3.8	0.6 $\pm$ 0.1	16
081126–2	6709.660	6709.928	Li I	3.7	0.7 $\pm$ 0.1	12
081126–3	6709.660	6709.953	Li I	3.8	0.6 $\pm$ 0.1	13
081127	6709.660	6709.794	Li I	3.9	0.6 $\pm$ 0.1	6
090106	6709.660	6709.946	Li I	3.0	0.5 $\pm$ 0.1	13
090110	6709.660	6709.913	Li I	3.0	0.4 $\pm$ 0.1	11
090111	6709.660	6709.995	Li I	2.9	0.5 $\pm$ 0.1	15
090305	6709.660	6709.753	Li I	3.1	0.8 $\pm$ 0.1	4
090531	6709.660	6709.769	Li I	3.2	0.8 $\pm$ 0.1	5
081126–1	7701.093	7701.091	K I	3.1	0.9 $\pm$ 0.1	0
081126–2	7701.093	7701.064	K I	3.1	0.9 $\pm$ 0.1	–1
081126–3	7701.093	7701.015	K I	3.1	0.9 $\pm$ 0.1	–3
081127	7701.093	7700.945	K I	3.3	0.7 $\pm$ 0.1	–6
090106	7701.093	7701.001	K I	5.4	–1.4 $\pm$ 0.1 <sup>c</sup>	–4
090110	7701.093	7700.869	K I	5.1	–1.2 $\pm$ 0.1 <sup>c</sup>	–9
090111	7701.093	7700.895	K I	5.1	–1.1 $\pm$ 0.1 <sup>c</sup>	–8
090305	7701.093	7701.001	K I	2.7	1.3 $\pm$ 0.1	–4
090531	7701.093	7700.891	K I	2.5	1.4 $\pm$ 0.1	–8
081126–1	8185.505	8185.689	Na I	3.2	1.1 $\pm$ 0.1	7
081126–2	8185.505	8185.622	Na I	3.3	0.9 $\pm$ 0.1	4
081126–3	8185.505	8185.611	Na I	3.2	1.0 $\pm$ 0.1	4
081127	8185.505	8185.532	Na I	3.8	1.0 $\pm$ 0.1	1
090106	8185.505	8185.748	Na I	3.2	1.0 $\pm$ 0.1	9
090110	8185.505	8185.533	Na I	3.8	1.0 $\pm$ 0.1	1
090111	8185.505	8185.732	Na I	3.3	1.0 $\pm$ 0.1	8
090305	8185.505	8185.439	Na I	3.9	0.9 $\pm$ 0.1	–2
090531	8185.505	8185.633	Na I	3.3	0.9 $\pm$ 0.1	5

<sup>a</sup>The integrated line fluxes are given in units of  $10^{-16}$  erg cm $^{-2}$  s $^{-1}$  and should only be used to calculate relative line fluxes between features in the same spectrum as our data are not photometrically calibrated and hence do not account for slit losses or non-photometric conditions.

<sup>b</sup>These velocities (km s $^{-1}$ ) are not corrected to the stellar rest frame ( $12.3 \pm 1.5$  km s $^{-1}$ ).

<sup>c</sup>This line is seen in emission.

Table 7. Derived NIR Magnitudes<sup>a</sup>, Colors<sup>a</sup>, Spectral Types, and  $A_v$  Values of TWA 30

UT <sup>b</sup>	$J$	$H$	$K_s$	$J - H$	$H - K_s$	$J - K_s$	NIR SpT <sup>c</sup>	$A_v$	Notes
990324	9.64	9.03	8.77	0.61	0.27	0.88	...	...	2MASS PSC
081204	10.2	9.3	8.8	0.91	0.43	1.34	M5	2.5	SpeX SXD
081215	10.5	9.6	9.2	0.85	0.41	1.25	M5	2.2	SpeX SXD
090202	9.8	9.0	8.7	0.75	0.35	1.09	M4.5	1.5	SpeX SXD
090514	11.3	10.2	9.6	1.09	0.61	1.71	M5.5	4.2	SpeX SXD
090515	11.7	10.5	9.7	1.23	0.75	1.98	M6	5.6	SpeX SXD
090520	12.7	11.0	10.0	1.68	0.95	2.63	M6	9.0	SpeX SXD
090616	10.6	9.6	9.2	0.91	0.47	1.39	M5	2.6	SpeX SXD
090628	10.6	9.7	9.2	0.96	0.49	1.45	...	...	SpeX prism
090629	10.5	9.6	9.1	0.99	0.48	1.47	...	...	SpeX prism
090629	10.5	9.5	9.1	0.93	0.48	1.41	M5	2.7	SpeX SXD

<sup>a</sup>All magnitudes and colors are derived using 2MASS filters for spectrophotometry on the NIR spectra taken in SXD or prism mode (as indicated) with the exception of the epoch marked '2MASS PSC,' which is photometry. In photometric conditions, the derived *absolute* spectrophotometry, flux calibrated with nearby A0 V stars, are accurate to ~10%, while the derived *relative* spectrophotometry (colors) are accurate to a few percent (Rayner et al. 2009). For a full description, see §3.3.1.

<sup>b</sup>UT dates are recorded as YYMMDD.

<sup>c</sup>All NIR SpT and  $A_v$  measurements were determined by dereddening the spectra to field M4-M8 templates and determining the best match; see §3.3.1.

Table 8. Selected Values of MagE Optical Data for TWA 30

UT Date <sup>a</sup>	Opt SpT <sup>b</sup>	$A_V$	$H\alpha^c$	[O I] $\lambda 6300^c$	[N II] $\lambda 6583^c$	[SII] $\lambda 6716^c$	Li I $\lambda 6708^c$	K I $\lambda 7699^c$
081126-1	M4.75	1.6	-8.0	-9.2	-0.6	-0.9	0.6	0.9
081127	M4.5	2.6	-8.1	-9.9	-0.5	-1.1	0.6	0.7
090106	M4	0.6	-6.8	-14.8 ± 0.3	-1.0	-2.6	0.5	-1.4
090110	M4	0.3	-6.8	-13.7	-0.8	-2.7	0.4	-1.2
090111	M4	0.2	-8.0	-13.4	-1.0	-2.5	0.5	-1.1
090305	M5.25	1.7	-4.6	-3.2	-0.3	-0.3	0.8	1.3
090531	M5.25	1.9	-5.6	-3.1	-0.4	-0.5	0.8	1.4

<sup>a</sup>UT dates are recorded as YYMMDD.

<sup>b</sup>These spectral types were determined from the dereddened data, described in §3.2.1 and shown graphically in Figure 6.

<sup>c</sup>The EW of the stated feature given in Å. The  $1\sigma$  uncertainty is 0.1 Å unless otherwise noted.

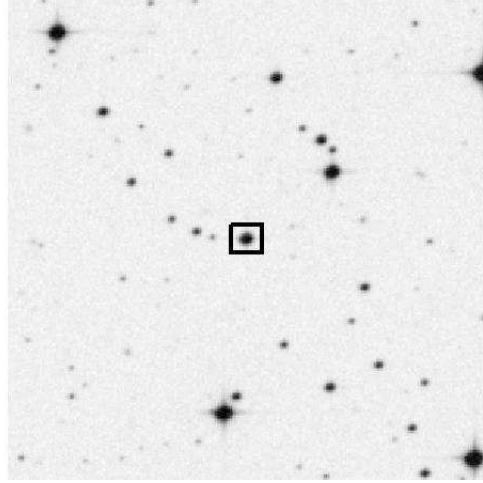


Fig. 1.— Finder chart for TWA 30. The field is centered on the target and is 5 arcmin on a side, with north up and east to the left. The image is in the  $R$ -band from the DSS II (epoch 1991 Feb 22 UT). A box of  $20''$  on a side marks the location of the target.

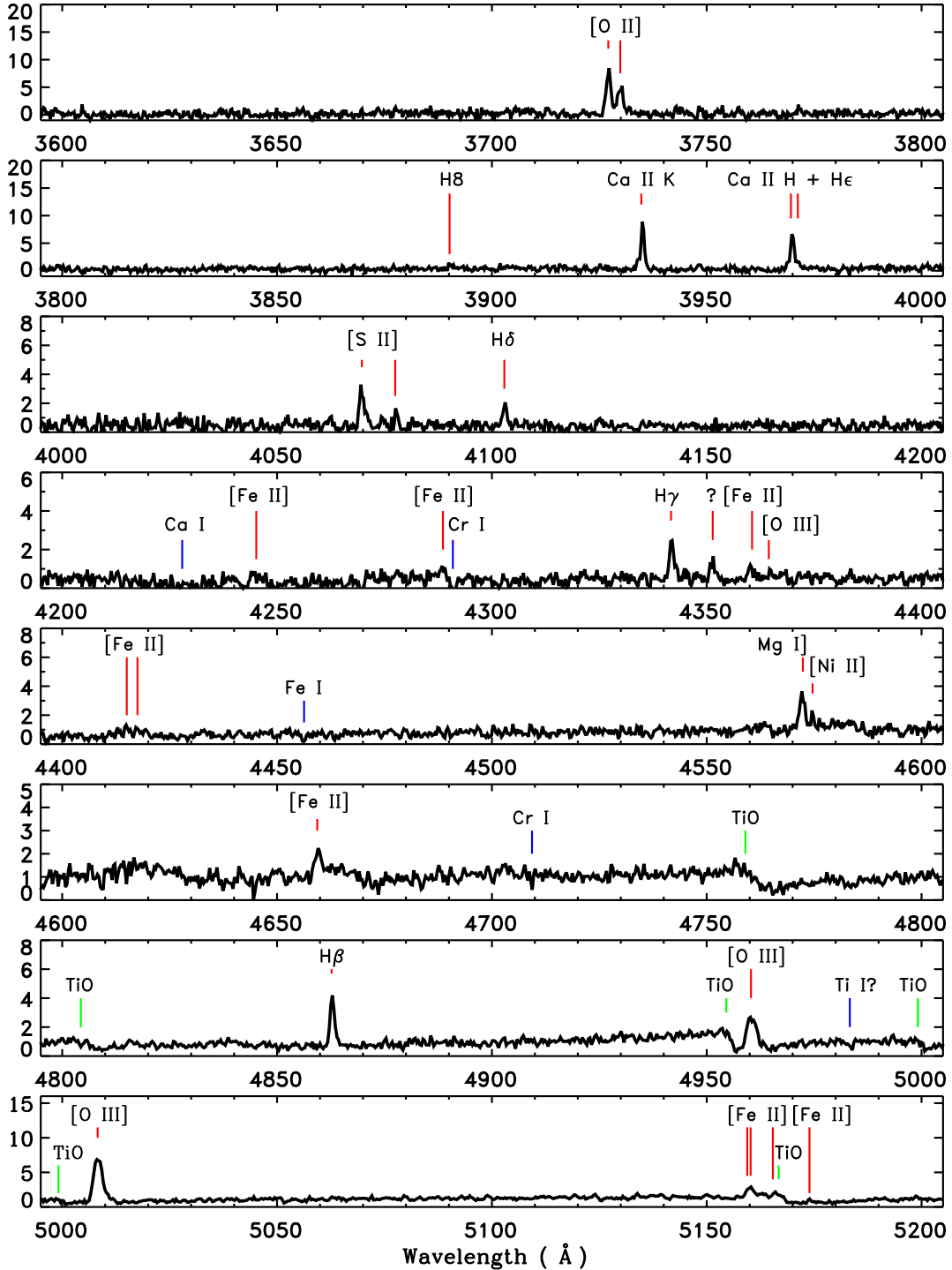


Fig. 2.— The optical spectrum of TWA 30, obtained with the MagE spectrograph on 2009 Jan 10 UT. Chromospheric emission lines and forbidden lines are indicated in red, absorption lines in blue, and molecular bands in green. Many forbidden lines typically associated with outflows (i.e., [O I], [O II], [S II]) are seen, along with strong Balmer line and Ca II emission, typical for stars with an active accretion disk. The spectral type derived from this observation is M4.

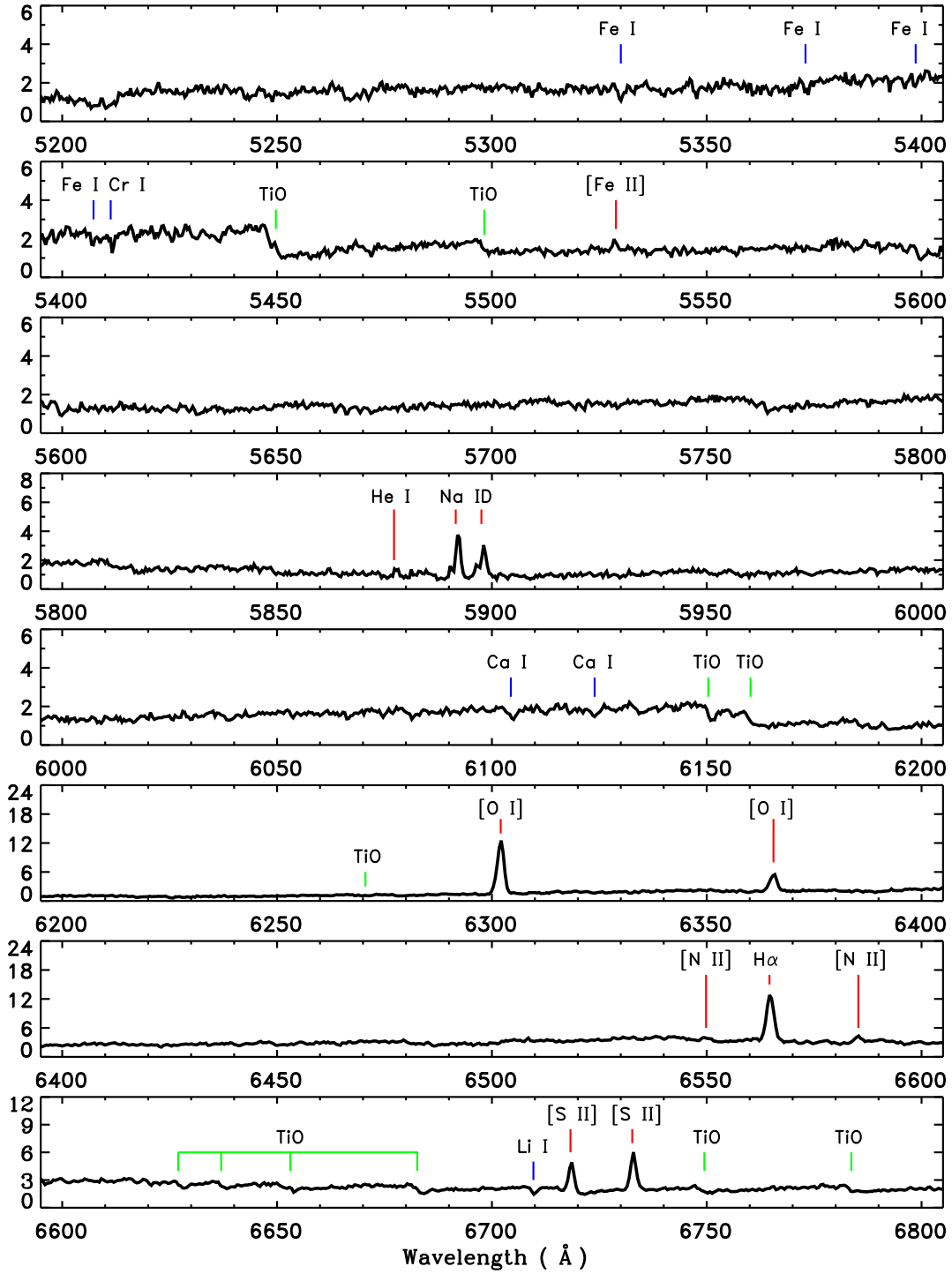


Fig. 3.— Same as Figure 2.

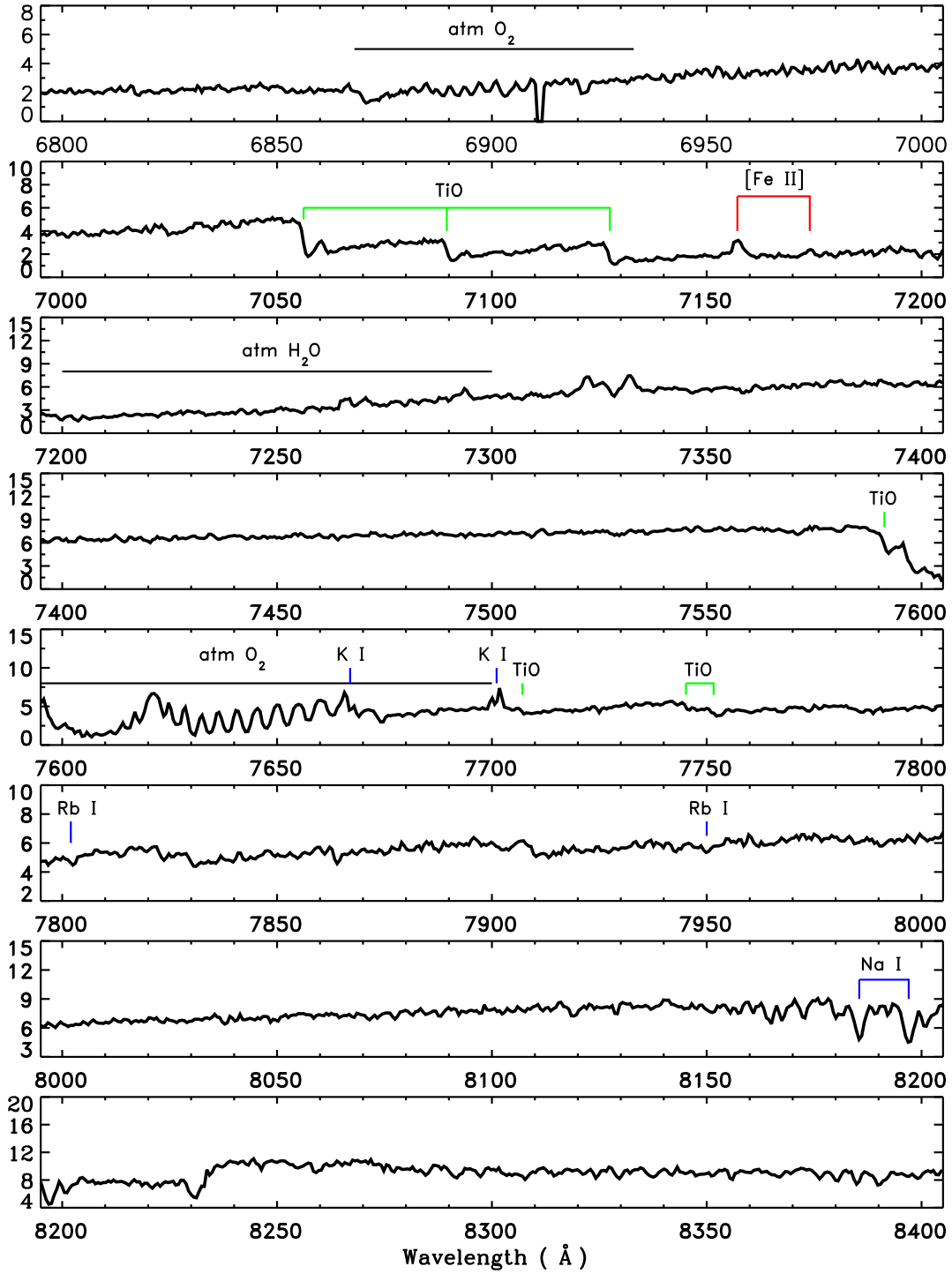


Fig. 4.— Same as Figure 2.

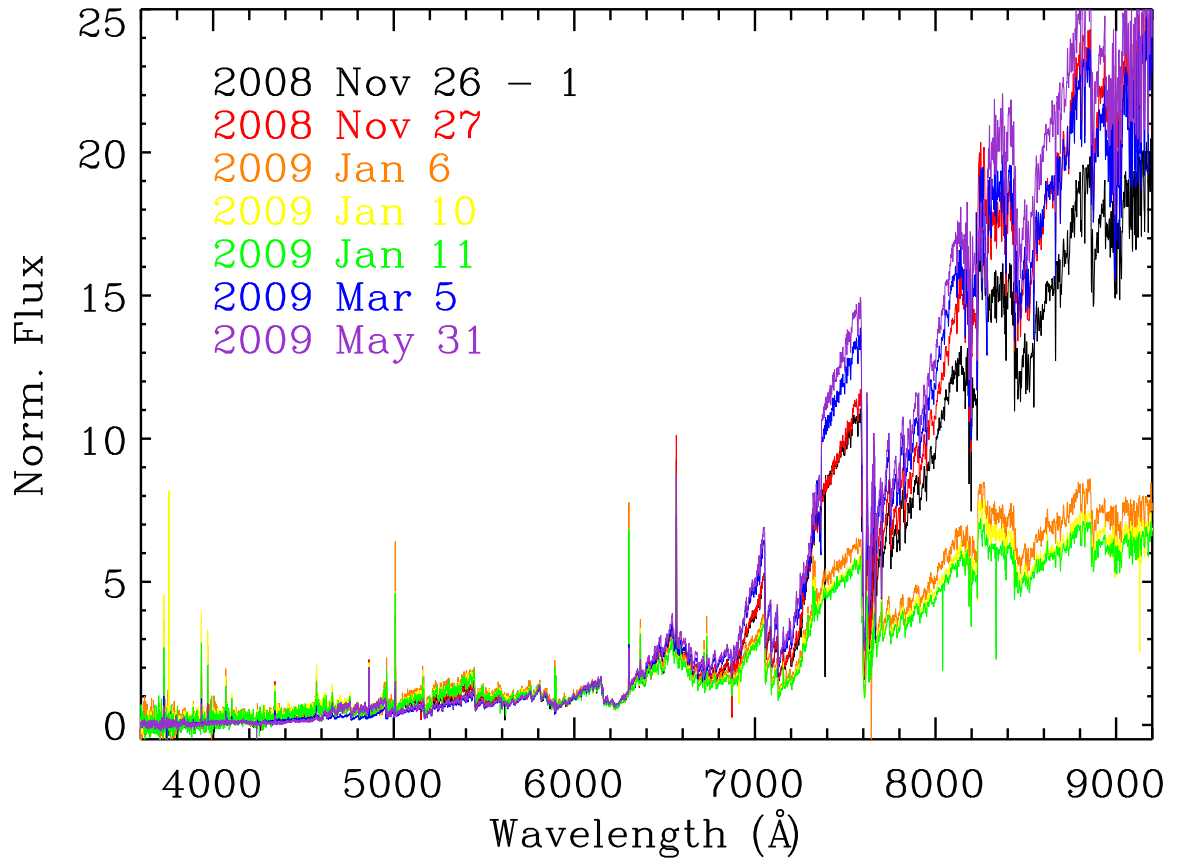


Fig. 5.— Optical spectra of TWA 30 taken with MagE at the seven indicated epochs. Three spectra were taken sequentially on 2008 Nov 26 UT, and we only show the first one here as all three are identical. The spectra have been normalized at 6000 Å, showing the highly variable nature of this object in both emission lines and the amount of reddening present.

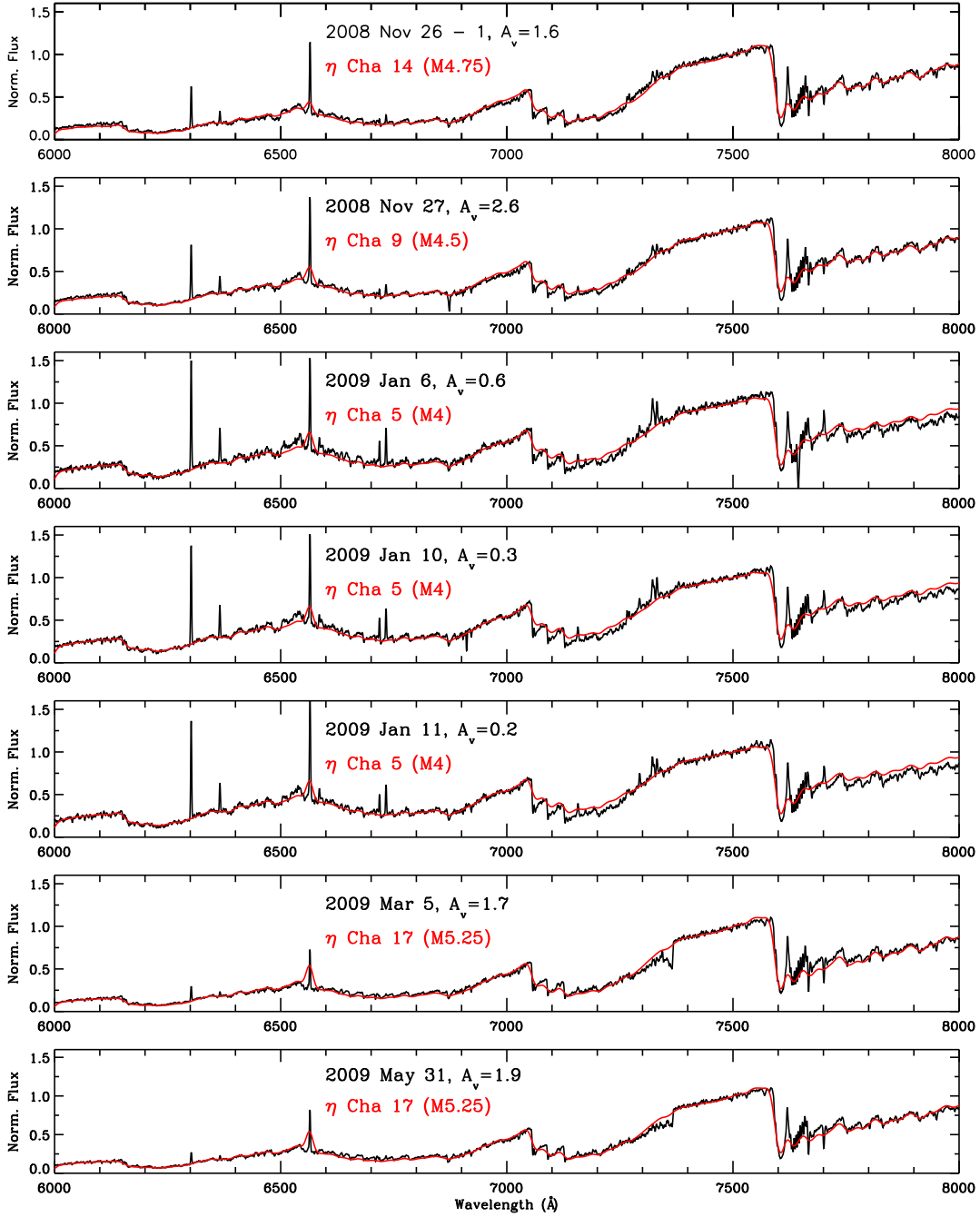


Fig. 6.— Overlays of the MagE optical spectra of TWA 30 (black;  $R \approx 4100$ ) at each stated epoch with optical  $\eta$  Cha templates (red;  $R \approx 1000$ , Luhman & Steeghs 2004), which provided the closest match for each epoch (see §3.2.1). The spectra have been dereddened by the stated amount to provide the best fit. All spectra have been normalized at  $7500 \text{ \AA}$ .

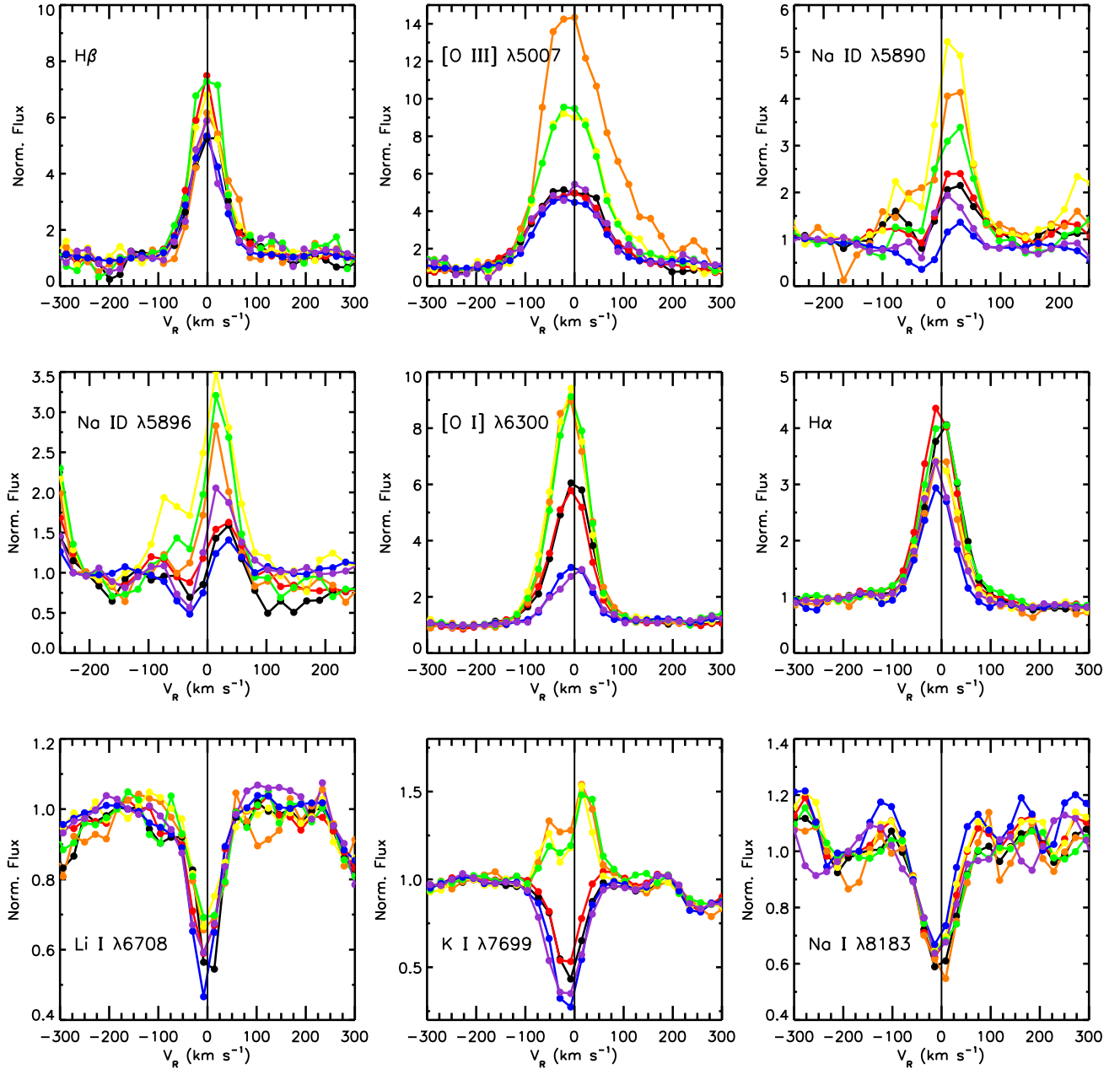


Fig. 7.— The radial velocity profiles of several prominent features in the seven MagE spectra, color-coded identically to that of Figure 5. For each panel, the flux has been normalized at  $-250$   $\text{km s}^{-1}$  and the star’s rest velocity ( $12.3$   $\text{km s}^{-1}$ ) has been subtracted out. Each feature is labeled in the inset. Note the P Cygni profiles of the Na I D lines in the 2009 Mar and May data and that the K I line goes into emission in the three 2009 Jan epochs.

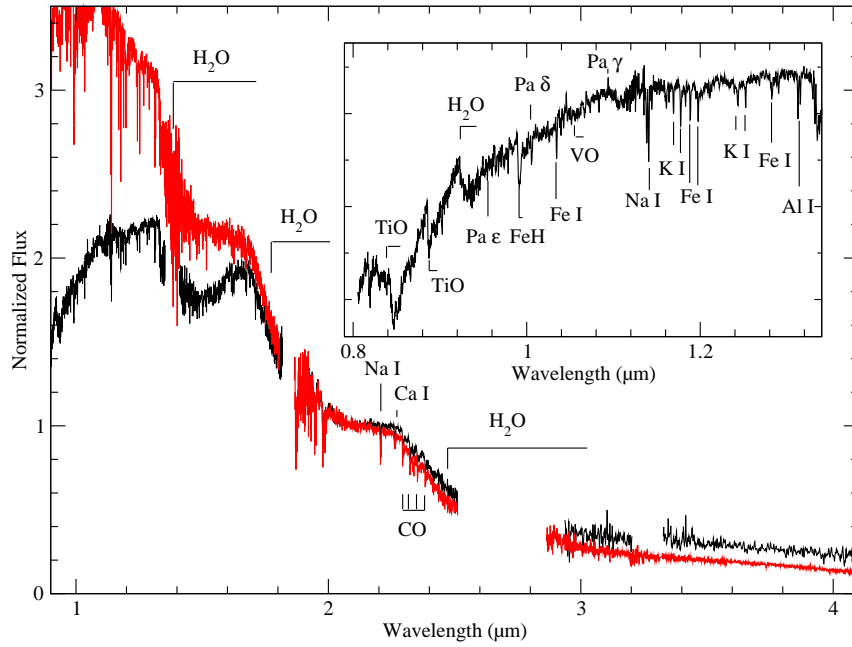


Fig. 8.— The SpeX SXD spectra of TWA 30 at the stated epochs. All spectra have been normalized at  $2.15 \mu\text{m}$ . The spectra have not been de-reddened. The spectrophotometry and colors calculated from these data are listed in Table 7.

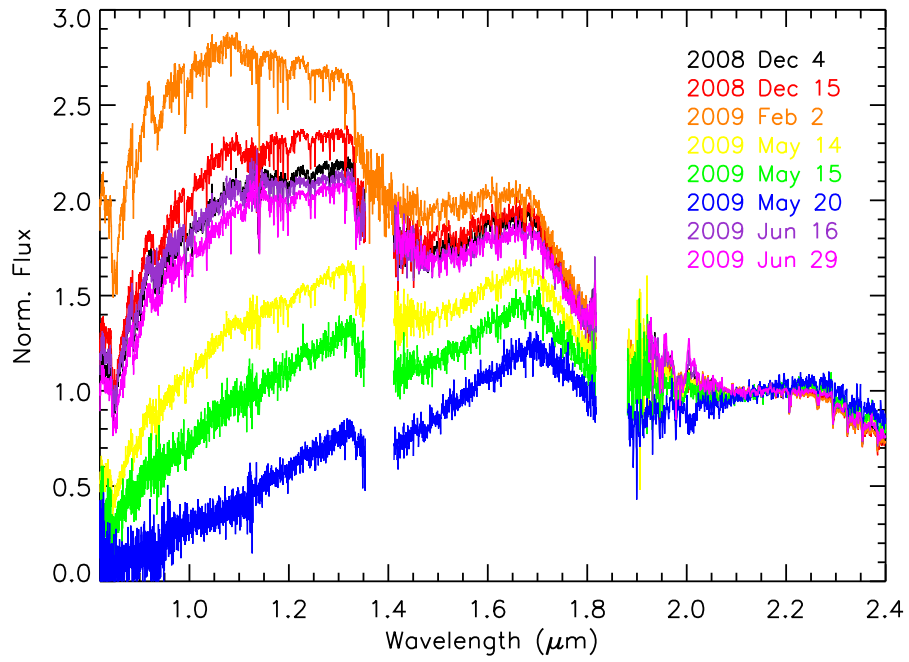


Fig. 9.— The combined SXD and LXD SpeX spectra of TWA 30 (black) obtained on 2008 Dec 4–5 UT shown in comparison to the M5 V field template Gl 51 (red). The spectrum of TWA 30 has not been de-reddened here or in the inset. Both spectra have been normalized at  $2.1 \mu\text{m}$ .

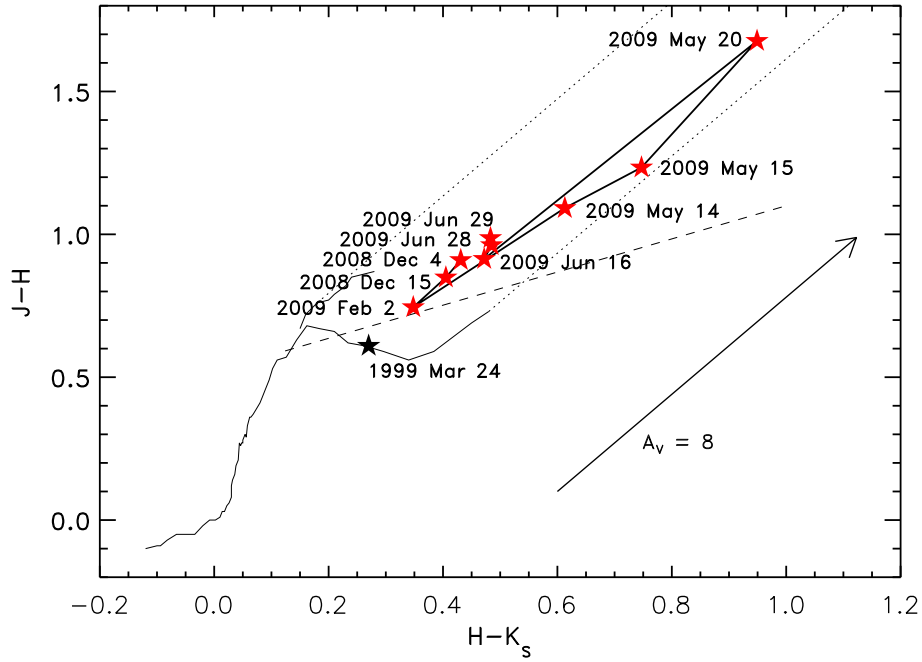


Fig. 10.— The NIR colors of TWA 30 at each epoch of our SpeX data (*red stars*; see Table 7) and one epoch (*black star*; 1999 Mar 24 UT) from the 2MASS PSC. The dwarf track ( $\geq M0$  from Leggett 1992; earlier types from Kenyon & Hartmann 1995) is the lower solid line and the giant track (Bessell & Brett 1988) is the upper solid line, the vectors for reddened dwarfs are shown as two dotted lines, the cTTS locus (Meyer et al. 1997) is shown as a single dashed line, and the arrow at the lower right indicates a reddening of  $A_v=8$ . Both the dwarf and giant tracks have been transformed to the CIT photometric system, which is similar to the 2MASS system (Carpenter 2001). The red stars are connected by a solid straight line to delineate the sequence of observations.

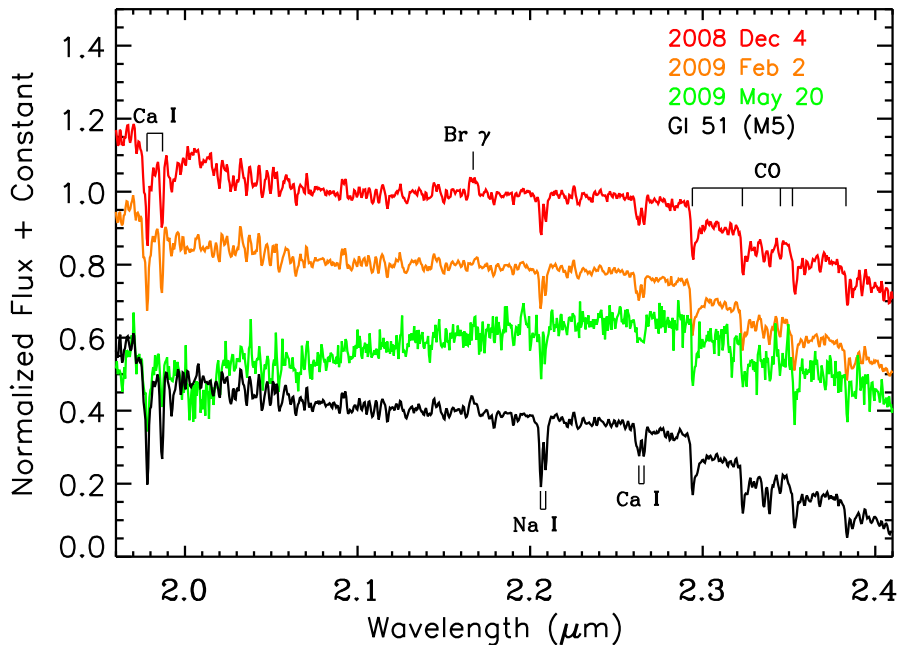


Fig. 11.— SpeX SXD spectra in the  $K$ -band region of TWA 30 at the three stated epochs (red, orange, green) shown in comparison to the M5 V field template Gl 51 (black). All spectra have been normalized at 2.15  $\mu\text{m}$  and are separated by constants of 0.2 along the y-axis. Note that the alkali doublet Na I is much stronger in the M5 template than in the spectra of TWA 30. Br  $\gamma$  is weakly present in the 2008 Dec 4 UT spectrum and in the Gl 51 template but is absent in the 2009 Feb 2 and 2009 May 20 data.

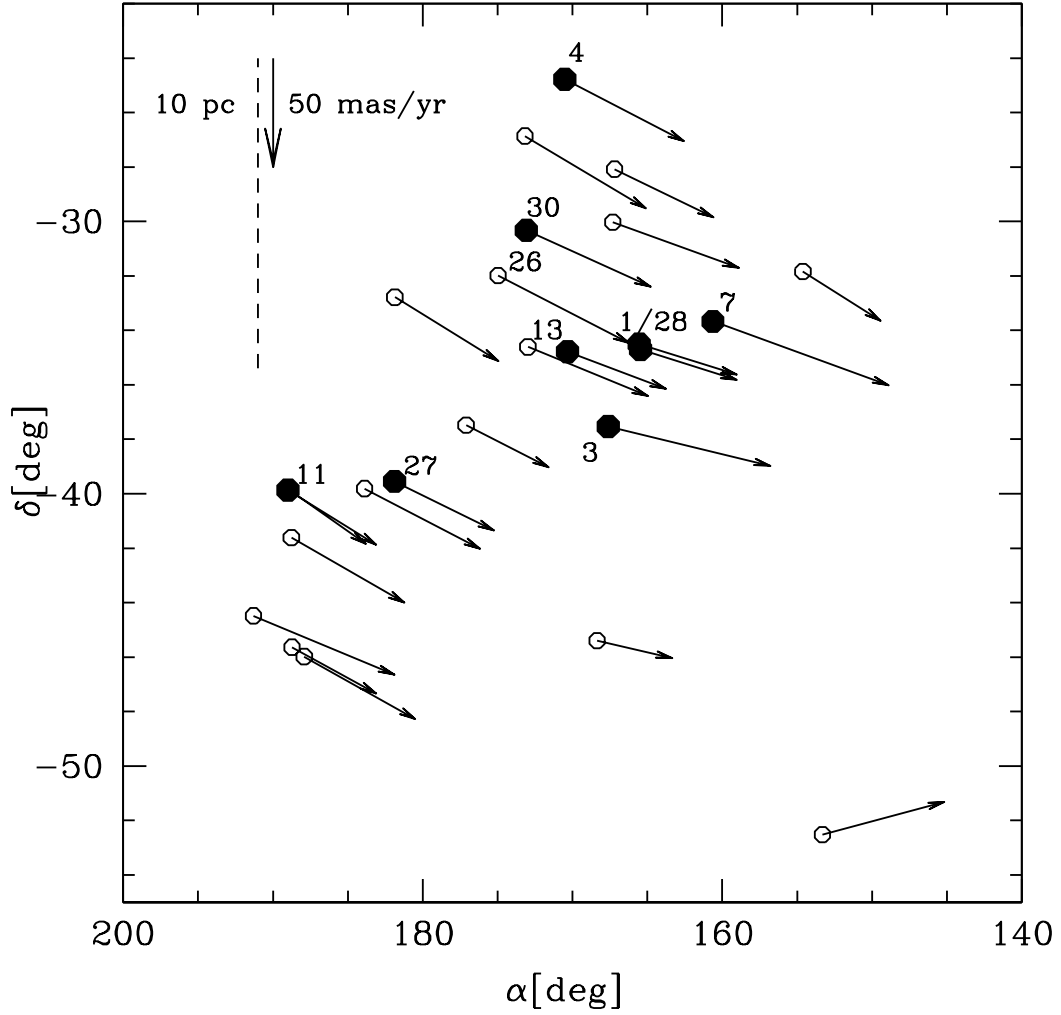


Fig. 12.— The spatial locations of all TWA members with disks (filled circles) and without disks (empty circles) based on mid-IR excesses, with the exception of TWA 30, which has no mid-IR data available but shows spectroscopic signs of a disk. Members with a disk are also labeled by their TWA designation. Note that most members with a disk reside in the north-west quadrant of the TWA. The short-dashed line marks a distance of 10 pc at the mean distance of the TWA members ( $53 \pm 3$  pc), and the arrow indicates the scale length for the proper motions of members.

## REFERENCES

- Adams, F. C., Lada, C. J., & Shu, F. H. 1987, *ApJ*, 312, 788
- Alexander, R. D., & Armitage, P. J. 2006, *ApJ*, 639, L83
- Appenzeller, I., & Mundt, R. 1989, *A&A Rev.*, 1, 291
- Baraffe, I., Chabrier, G., Allard, F., & Hauschildt, P. H. 1998, *A&A*, 337, 403
- Barrado y Navascués, D. 2006, *A&A*, 459, 511
- Bernstein, R., Shtetman, S. A., Gunnels, S. M., Mochnacki, S., & Athey, A. E. 2003, in *Society of Photo-Optical Instrumentation Engineers (SPIE) Conference Series*, Vol. 4841, *Society of Photo-Optical Instrumentation Engineers (SPIE) Conference Series*, ed. M. Iye & A. F. M. Moorwood, 1694–1704
- Bessell, M. S., & Brett, J. M. 1988, *PASP*, 100, 1134
- Biller, B. A., & Close, L. M. 2007, *ApJ*, 669, L41
- Bochanski, J. J., et al. 2009, *PASP*, 121, 1409
- Bochanski, J. J., West, A. A., Hawley, S. L., & Covey, K. R. 2007, *AJ*, 133, 531
- Böhm, K.-H. 1995, *Ap&SS*, 233, 11
- Bourke, T. L., Crapsi, A., Myers, P. C., Evans, II, N. J., Wilner, D. J., Huard, T. L., Jørgensen, J. K., & Young, C. H. 2005, *ApJ*, 633, L129
- Bouvier, J., et al. 2007, *A&A*, 463, 1017
- . 1999, *A&A*, 349, 619
- . 2003, *A&A*, 409, 169
- Brandeker, A., Jayawardhana, R., & Najita, J. 2003, *AJ*, 126, 2009
- Calvet, N., Muzerolle, J., Briceño, C., Hernández, J., Hartmann, L., Saucedo, J. L., & Gordon, K. D. 2004, *AJ*, 128, 1294
- Cardelli, J. A., Clayton, G. C., & Mathis, J. S. 1989, *ApJ*, 345, 245
- Carpenter, J. M. 2001, *AJ*, 121, 2851
- Chabrier, G., & Baraffe, I. 2000, *ARA&A*, 38, 337
- Chambers, J. E. 2004, *Earth and Planetary Science Letters*, 223, 241

- Chauvin, G., Lagrange, A.-M., Dumas, C., Zuckerman, B., Mouillet, D., Song, I., Beuzit, J.-L., & Lowrance, P. 2004, *A&A*, 425, L29
- Cruz, K. L., Kirkpatrick, J. D., & Burgasser, A. J. 2009, *AJ*, 137, 3345
- Cushing, M. C., Vacca, W. D., & Rayner, J. T. 2004, *PASP*, 116, 362
- Cutri, R. M., et al. 2003, *VizieR Online Data Catalog*, 2246, 0
- de la Reza, R., Torres, C. A. O., Quast, G., Castilho, B. V., & Vieira, G. L. 1989, *ApJ*, 343, L61
- Delfosse, X., Forveille, T., Perrier, C., & Mayor, M. 1998, *A&A*, 331, 581
- Ducourant, C., Teixeira, R., Chauvin, G., Daigne, G., Le Campion, J.-F., Song, I., & Zuckerman, B. 2008, *A&A*, 477, L1
- Edwards, S. 2007, in *IAU Symposium*, Vol. 243, *IAU Symposium*, ed. J. Bouvier & I. Appenzeller, 171–182
- Edwards, S., Fischer, W., Kwan, J., Hillenbrand, L., & Dupree, A. K. 2003, *ApJ*, 599, L41
- Enoch, M. L., Evans, II, N. J., Sargent, A. I., Glenn, J., Rosolowsky, E., & Myers, P. 2008, *ApJ*, 684, 1240
- Epchtein, N., et al. 1997, *The Messenger*, 87, 27
- Ercolano, B., Drake, J. J., Raymond, J. C., & Clarke, C. C. 2008, *ApJ*, 688, 398
- Fedele, D., van den Ancker, M. E., Henning, T., Jayawardhana, R., & Oliveira, J. M. 2009, *ArXiv e-prints*
- Fernández, M., & Comerón, F. 2001, *A&A*, 380, 264
- Finch, C. T., Zacharias, N., & Wycoff, G. L. 2010, *ArXiv e-prints*
- Fleming, T. A., Schmitt, J. H. M. M., & Giampapa, M. S. 1995, *ApJ*, 450, 401
- Gizis, J. E. 2002, *ApJ*, 575, 484
- Gizis, J. E., Jao, W.-C., Subasavage, J. P., & Henry, T. J. 2007, *ApJ*, 669, L45
- Golimowski, D. A., et al. 2004, *AJ*, 127, 3516
- Gregorio-Hetem, J., Lepine, J. R. D., Quast, G. R., Torres, C. A. O., & de La Reza, R. 1992, *AJ*, 103, 549
- Güdel, M., et al. 2007, *A&A*, 468, 353
- Hambly, N. C., Davenhall, A. C., Irwin, M. J., & MacGillivray, H. T. 2001a, *MNRAS*, 326, 1315

- Hambly, N. C., Irwin, M. J., & MacGillivray, H. T. 2001b, *MNRAS*, 326, 1295
- Hambly, N. C., et al. 2001c, *MNRAS*, 326, 1279
- Hartigan, P. 1989, *ApJ*, 339, 987
- Hartigan, P., Edwards, S., & Ghandour, L. 1995, *ApJ*, 452, 736
- Hartmann, L. 1998, *Accretion Processes in Star Formation*, ed. L. Hartmann
- Henize, K. G. 1976, *ApJS*, 30, 491
- Herbig, G. H. 1978, *Can Post-T Tauri Stars Be Found? (Problems of Physics and Evolution of the Universe)*, 171–+
- . 1990, *ApJ*, 360, 639
- Herczeg, G. J., Cruz, K. L., & Hillenbrand, L. A. 2009, *ApJ*, 696, 1589
- Herczeg, G. J., & Hillenbrand, L. A. 2008, *ApJ*, 681, 594
- Hirth, G. A., Mundt, R., & Solf, J. 1997, *A&AS*, 126, 437
- Jayawardhana, R., Hartmann, L., Fazio, G., Fisher, R. S., Telesco, C. M., & Piña, R. K. 1999, *ApJ*, 521, L129
- Johns, C. M., & Basri, G. 1995, *ApJ*, 449, 341
- Johnson, D. R. H., & Soderblom, D. R. 1987, *AJ*, 93, 864
- Kamiński, T., Schmidt, M., Tyłenda, R., Konacki, M., & Gromadzki, M. 2009, *ApJS*, 182, 33
- Kastner, J. H., Zuckerman, B., Weintraub, D. A., & Forveille, T. 1997, *Science*, 277, 67
- Kenyon, S. J., & Hartmann, L. 1995, *ApJS*, 101, 117
- Kirkpatrick, J. D., Barman, T. S., Burgasser, A. J., McGovern, M. R., McLean, I. S., Tinney, C. G., & Lowrance, P. J. 2006, *ApJ*, 639, 1120
- Kirkpatrick, J. D., Henry, T. J., & McCarthy, Jr., D. W. 1991, *ApJS*, 77, 417
- Kwan, J., Edwards, S., & Fischer, W. 2007, *ApJ*, 657, 897
- Lawson, W. A., & Crause, L. A. 2005, *MNRAS*, 357, 1399
- Lawson, W. A., Crause, L. A., Mamajek, E. E., & Feigelson, E. D. 2001, *MNRAS*, 321, 57
- Leggett, S. K. 1992, *ApJS*, 82, 351
- Looper, D. L., Burgasser, A. J., Kirkpatrick, J. D., & Swift, B. J. 2007, *ApJ*, 669, L97

- Low, F. J., Smith, P. S., Werner, M., Chen, C., Krause, V., Jura, M., & Hines, D. C. 2005, *ApJ*, 631, 1170
- Luhman, K. L. 1999, *ApJ*, 525, 466
- . 2004, *ApJ*, 616, 1033
- Luhman, K. L., & Muench, A. A. 2008, *ApJ*, 684, 654
- Luhman, K. L., Stauffer, J. R., Muench, A. A., Rieke, G. H., Lada, E. A., Bouvier, J., & Lada, C. J. 2003, *ApJ*, 593, 1093
- Luhman, K. L., & Steeghs, D. 2004, *ApJ*, 609, 917
- Mamajek, E. E. 2005, *ApJ*, 634, 1385
- Mamajek, E. E., Lawson, W. A., & Feigelson, E. D. 1999, *ApJ*, 516, L77
- Marshall, J. L., et al. 2008, in *Society of Photo-Optical Instrumentation Engineers (SPIE) Conference Series*, Vol. 7014, *Society of Photo-Optical Instrumentation Engineers (SPIE) Conference Series*
- Martín, E. L., Basri, G., & Zapatero Osorio, M. R. 1999, *AJ*, 118, 1005
- Masciadri, E., & Raga, A. C. 2004, *ApJ*, 615, 850
- Meyer, M. R., Calvet, N., & Hillenbrand, L. A. 1997, *AJ*, 114, 288
- Mohanty, S., & Basri, G. 2003, *ApJ*, 583, 451
- Mohanty, S., Jayawardhana, R., & Barrado y Navascués, D. 2003, *ApJ*, 593, L109
- Mohanty, S., Jayawardhana, R., & Basri, G. 2005, *ApJ*, 626, 498
- Monet, D., & et al. 1998, *VizieR Online Data Catalog*, 1252, 0
- Monet, D. G., et al. 2003, *AJ*, 125, 984
- Morrow, A. L., et al. 2008, *ApJ*, 676, L143
- Murray, C. A. 1989, *A&A*, 218, 325
- Muzerolle, J., Hillenbrand, L., Calvet, N., Briceño, C., & Hartmann, L. 2003, *ApJ*, 592, 266
- Muzerolle, J., Hillenbrand, L., Calvet, N., Hartmann, L., & Briceño, C. 2001, in *Astronomical Society of the Pacific Conference Series*, Vol. 244, *Young Stars Near Earth: Progress and Prospects*, ed. R. Jayawardhana & T. Greene, 245–+
- Natta, A., Testi, L., Muzerolle, J., Randich, S., Comerón, F., & Persi, P. 2004, *A&A*, 424, 603

- Nelson, L. A., Rappaport, S., & Chiang, E. 1993, *ApJ*, 413, 364
- O'Donnell, J. E. 1994, *ApJ*, 422, 158
- Phan-Bao, N., et al. 2008, *ApJ*, 689, L141
- Plavchan, P., Werner, M. W., Chen, C. H., Stapelfeldt, K. R., Su, K. Y. L., Stauffer, J. R., & Song, I. 2009, *ApJ*, 698, 1068
- Raga, A. C., Böhm, K.-H., & Cantó, J. 1996, *Revista Mexicana de Astronomia y Astrofisica*, 32, 161
- Rayner, J. T., Cushing, M. C., & Vacca, W. D. 2009, *ApJS*, 185, 289
- Rayner, J. T., Toomey, D. W., Onaka, P. M., Denault, A. J., Stahlberger, W. E., Vacca, W. D., Cushing, M. C., & Wang, S. 2003, *PASP*, 115, 362
- Reiners, A. 2009, *ApJ*, 702, L119
- Riaz, B., & Gizis, J. E. 2008, *ApJ*, 681, 1584
- Riaz, B., Gizis, J. E., & Hmiel, A. 2006, *ApJ*, 639, L79
- Rieke, G. H., & Lebofsky, M. J. 1985, *ApJ*, 288, 618
- Rucinski, S. M., & Krautter, J. 1983, *A&A*, 121, 217
- Scholz, R.-D., McCaughrean, M. J., Zinnecker, H., & Lodieu, N. 2005, *A&A*, 430, L49
- Schwartz, R. D. 1983, *ARA&A*, 21, 209
- Shu, F. H., Adams, F. C., & Lizano, S. 1987, *ARA&A*, 25, 23
- Skrutskie, M. F., et al. 2006, *AJ*, 131, 1163
- Soderblom, D. R., et al. 1998, *ApJ*, 498, 385
- Song, I., Zuckerman, B., & Bessell, M. S. 2003, *ApJ*, 599, 342
- Sterzik, M. F., Alcalá, J. M., Covino, E., & Petr, M. G. 1999, *A&A*, 346, L41
- Sterzik, M. F., Pascucci, I., Apai, D., van der Blik, N., & Dullemond, C. P. 2004, *A&A*, 427, 245
- Tachihara, K., Neuhauser, R., & Fukui, Y. 2009, *PASJ*, 61, 585
- Terquem, C., & Papaloizou, J. C. B. 2000, *A&A*, 360, 1031
- Torres, C. A. O., Quast, G. R., Melo, C. H. F., & Sterzik, M. F. 2008, *Young Nearby Loose Associations*, ed. Reipurth, B., 757–+

- Vacca, W. D., Cushing, M. C., & Rayner, J. T. 2003, *PASP*, 115, 389
- van der Blik, N. S., et al. 2004, in *Society of Photo-Optical Instrumentation Engineers (SPIE) Conference Series*, Vol. 5492, *Society of Photo-Optical Instrumentation Engineers (SPIE) Conference Series*, ed. A. F. M. Moorwood & M. Iye, 1582–1589
- van Leeuwen, F. 2007, *A&A*, 474, 653
- Voges, W., et al. 1999, *A&A*, 349, 389
- . 2000, *IAU Circ.*, 7432, 3
- Webb, R. A., Zuckerman, B., Platais, I., Patience, J., White, R. J., Schwartz, M. J., & McCarthy, C. 1999, *ApJ*, 512, L63
- Weingartner, J. C., & Draine, B. T. 2001, *ApJ*, 548, 296
- Weintraub, D. A., Saumon, D., Kastner, J. H., & Forveille, T. 2000, *ApJ*, 530, 867
- West, A. A., & Basri, G. 2009, *ApJ*, 693, 1283
- West, A. A., Hawley, S. L., Bochanski, J. J., Covey, K. R., Reid, I. N., Dhital, S., Hilton, E. J., & Masuda, M. 2008, *AJ*, 135, 785
- Whelan, E. T., Ray, T. P., & Bacciotti, F. 2009, *ApJ*, 691, L106
- Whelan, E. T., Ray, T. P., Bacciotti, F., Natta, A., Testi, L., & Randich, S. 2005, *Nature*, 435, 652
- Whelan, E. T., Ray, T. P., Randich, S., Bacciotti, F., Jayawardhana, R., Testi, L., Natta, A., & Mohanty, S. 2007, *ApJ*, 659, L45
- White, R. J., & Basri, G. 2003, *ApJ*, 582, 1109
- White, R. J., & Ghez, A. M. 2001, *ApJ*, 556, 265
- Wyatt, M. C., Dent, W. R. F., & Greaves, J. S. 2003, *MNRAS*, 342, 876
- Zuckerman, B., & Song, I. 2004, *ARA&A*, 42, 685
- Zuckerman, B., Webb, R. A., Schwartz, M., & Becklin, E. E. 2001, *ApJ*, 549, L233